

Continent–ocean transition and voluminous magmatic underplating derived from *P*-wave velocity modelling of the East Greenland continental margin

Max Voss and Wilfried Jokat

Alfred Wegener Institute for Polar and Marine Research, Columbusstrasse, 27568 Bremerhaven, Germany. E-mail: Max.Voss@awi.de (MV)

Accepted 2007 March 12. Received 2007 January 15; in original form 2006 September 2

SUMMARY

Deep seismic refraction data were gathered across the entire East Greenland rifted margin north of the Jan Mayen Fracture Zone between 72°N and 75°N in 2003. Investigations of the deep crustal structure of this continental margin provide constraints on the formation of the margin and its structural evolution during and after late Cretaceous–early Tertiary rifting and continental break-up. We present here the results along two profiles located in the prolongation of the Godthåb Gulf and the Kejser Franz Joseph Fjord. Regional *P*-wave velocity models were derived from forward traveltimes modelling of land stations and ocean bottom hydrophone (OBH) recordings. For the first time, long deep seismic sounding transects off East Greenland provide a full insight into the crustal architecture of the transition from continental to oceanic crust. A mean result is the identification of voluminous magmatic underplating, which is wider and thicker than previously thought. *P*-wave velocities of the underplated material range between 7.1 and 7.4 km s^{−1} and the horizontal extents on the profiles are 225 and 190 km. The maximum thickness of the underplated material is 15–16 km. Furthermore, the *P*-wave velocity models reveal a 120–130 km wide continent–ocean transition zone (COT), based on an interpretation of the extent of Cretaceous syn-rift sediments mixed with basaltic intrusions and the lateral increase of velocities in the crustal layers. Excess magmatism must have been present during a long-term rifting process, accompanying the extension of the continental crust and giving rise to the voluminous magmatic underplating. A consequence of our interpretation of the seismic refraction data is a likely rift propagation in the Greenland Sea from north to south. Additionally, a comparison of *P*-wave velocity models of the East Greenland Margin and Vøring Margin reveals significantly asymmetric crustal architectures. The voluminous magmatic underplating and asymmetrical conjugate margins formations are considered as a mirror of complex pre- and syn-rift processes.

Key words: crustal structure, East Greenland, ray tracing, rifted margin, underplating.

1 INTRODUCTION

The East Greenland continental margin is bounded landwards between the Jan Mayen and Greenland fracture zones by the Caledonian fold belt, formed in Silurian times (Escher & Pulvertaft 1995; Henriksen *et al.* 2000) and Devonian sedimentary basins developed during the ensuing extensional collapse (Fig. 1). Subsequently, sedimentary basin formation took place during a long-term Mesozoic rifting process that terminated in Tertiary magmatism generally related to the Iceland hotspot and the break-up of the North Atlantic. Onshore outcrops of igneous rocks prove this on Hold with Hope, Wollaston Foreland and Shannon Island. Here, the lavas reach 800 m in thickness (Upton *et al.* 1980; Upton 1988). South of the Jan Mayen Fracture Zone, much larger amounts of flood basalts are found onshore on the Geikie Plateau, and there is

evidence for the erosion and removal of a thick pile of basaltic lavas on Jameson Land (Larsen & Marcussen 1992; Saunders *et al.* 1997). Modelling of wide-angle seismic data, from Shannon Island to the Scoresby Sund area, have also given evidence for varying intensities of Tertiary magmatic activity offshore from north to south. Crustal structure models along the margin reveal variations in the Moho topography (Weigel *et al.* 1995; Fechner & Jokat 1996; Mandler & Jokat 1998; Schlindwein & Jokat 1999). Seaward dipping reflector sequences (SDRs) (Hinz *et al.* 1987) and high velocity bodies in the lower crust, with *P*-wave velocities of more than 7.0 km s^{−1} (Mutter & Zehnder 1988; White & McKenzie 1989; Schlindwein & Jokat 1999) are reported north of the Jan Mayen Fracture Zone. However, south of Kong Oscar Fjord, deep seismic data provide no evidence of such a high velocity lower crust (Schlindwein & Jokat 1999; Schmidt-Aursch & Jokat 2005a). The

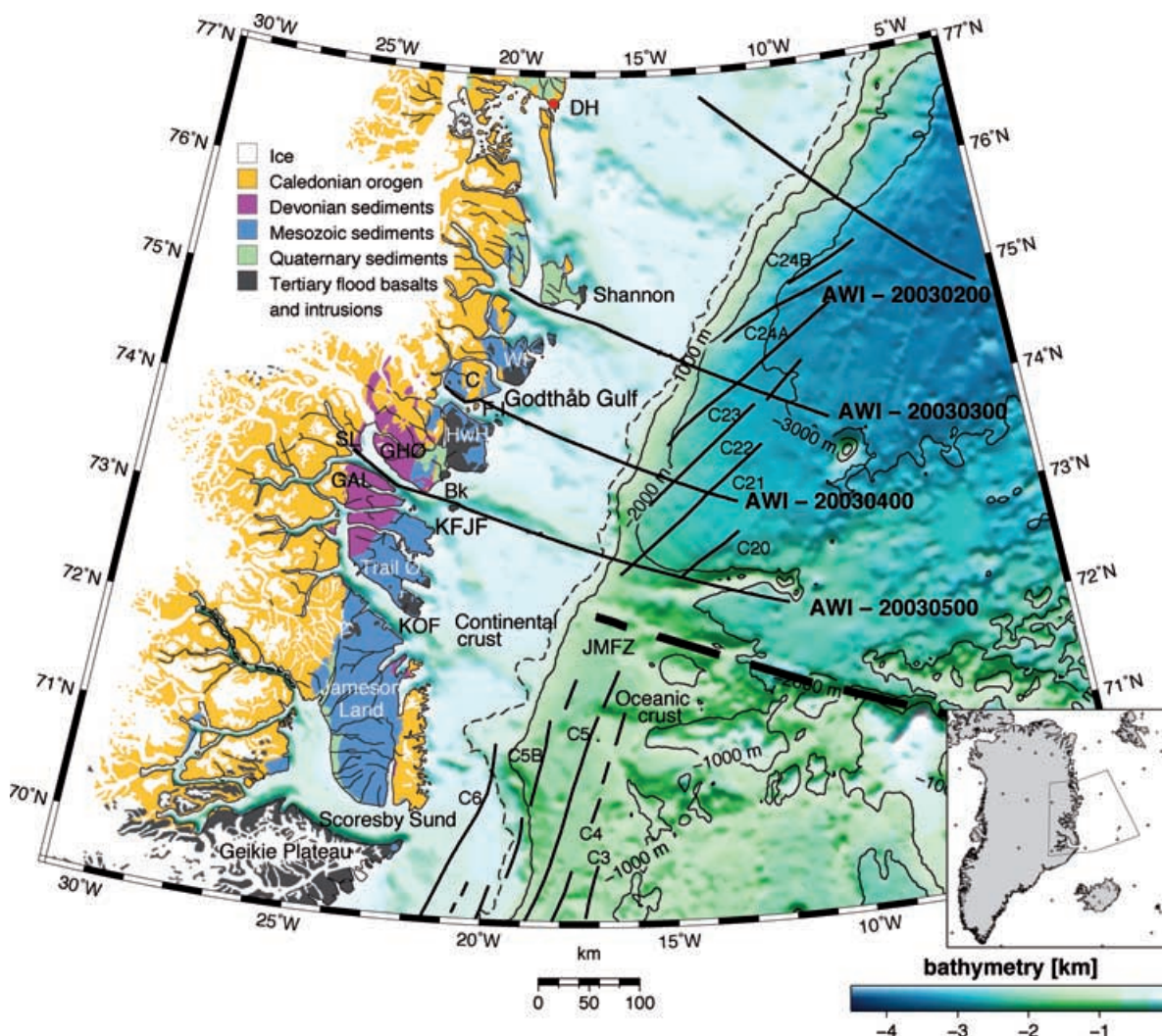


Figure 1. Simplified geological map of East Greenland Fjord Region after *Escher and Pulvertaft* (Escher & Pulvertaft 1995) (copyright Geological Survey of Denmark and Greenland) and *Henriksen et al.* (2000). IBCAO Bathymetry after *Jakobsson et al.* (2000). Bk: Bontekoe Ø. C: Clavering Ø. DH: Danmarkshavn (magnetic base station). F.I.: Finsch Island. GAL: Gunnar Anderson Land. GHØ: Gauss Halvø. HwH: Hold with Hope. JMFZ: Jan Mayen Fracture Zone. KFJF: Keiser Franz Joseph Fjord. KOF: Kong Oscar Fjord. SL: Strindberg Land. WF: Wolaston Foreland. All seismic profiles acquired in 2003 shown as thick solid black lines. Thin solid black lines mark ocean spreading anomalies. Thick dashed line represents the location of JMFZ as reference. Thin dashed line marks the smoothed shelf edge (330 m). Scale is valid for 73°N.

total melt production north of the Jan Mayen Fracture Zone remained unresolved from these studies, because sea ice cover prevented the transects from crossing the entire shelf and continental margin into the normal oceanic realm. Thus, the seaward and northward extent of magmatic underplating seen partly on seismic profiles of Kong Oscar Fjord and Keiser Franz Joseph Fjord are the subject of debate (Schlindwein & Jokat 1999; Schmidt-Aursch & Jokat 2005a). Seismic data from the conjugate Vøring Margin off Norway (Mjelde *et al.* 1997; Mjelde *et al.* 2001; Raum *et al.* 2002; Mjelde *et al.* 2005), on the other hand, revealed extensive magmatic underplating and thickened oceanic crust, which would support models of larger than known underplating for the East Greenland Margin. The location of the continent–ocean boundary (COB) in this part of the East Greenland margin is the subject of further controversy. Until now, the deeper crustal structure of the continental margin off East Greenland was unknown, with suggestions based instead on short seismic transects and/or potential field data. No seismic profiles, imaging the deeper crustal structure, were available, which would

provide constraints for an unambiguous continent–ocean transition (COT). Hinz *et al.* (1987) showed seaward dipping reflector sequences on multichannel seismic profiles, and argued for a coincidence of the COB and SDRs in consideration of the eruption of massive volcanic sequences over highly extended continental crust during the latest phases of rifting prior to seafloor spreading (Hinz 1981). Escher & Pulvertaft (1995) established the COB based on the coincidence of a gravity high with the bathymetric shelf margin, and using magnetic data. Scott (2000) suggested that anomaly C23 can be traced into the previously interpreted continental crust and placed the COB further west, about 10 km off the East Greenland coastline. He interpreted the ambiguous magnetic pattern between the old COB and the coastline as oceanic spreading anomalies. Tsikalas *et al.* (2002) based their location of the COB on reconstruction models and reinterpretation of the magnetic lineations. Those authors proposed C22 to be the oldest confidently identifiable magnetic anomaly and placed the COB 50–80 km East of that of Scott (2000).

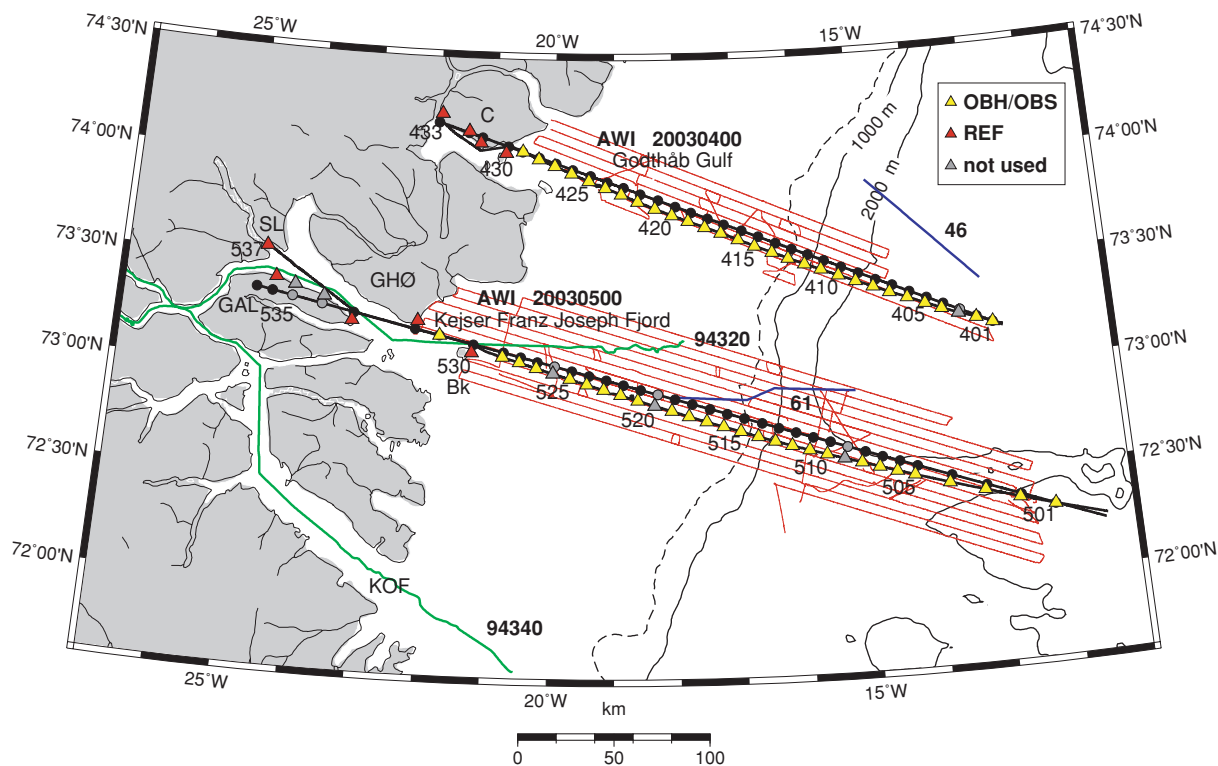


Figure 2. Location of the Godthåb Gulf and Keiser Franz Joseph Fjord seismic refraction profiles. Red lines show flight lines of the airborne magnetic survey. Yellow triangles show locations of the OBS/OBS, red triangles represent locations of REF land stations. Black dots show the locations of the receivers projected onto the straight line, as described in the text. Gray triangles and dots mark unused receiver stations. First, last and every fifth location are labelled. Green lines represent seismic refraction profiles after Schlindwein & Jokat (1999); blue lines mark multi channel seismic profiles after Hinz *et al.* (1987). For additional labels see Fig. 1. Scale is valid for 73°N.

To investigate the deeper crustal structure and the transition from continental to oceanic crust between the Jan Mayen and Greenland fracture zones (Jokat *et al.* 2004) new seismic refraction data across the East Greenland Margin were acquired by the Alfred Wegener Institute for Polar and Marine Research (AWI) using R/V *Polarstern* in 2003. This paper presents forward modelling of *P*-wave arrivals recorded by onshore receivers and ocean bottom seismometers on the two southernmost profiles, which are conjugate to the Vøring Plateau. The southern transect, AWI-20030500, extended an earlier profile (94320) along the Keiser Franz Joseph Fjord (Schlindwein & Jokat 1999) (Figs 1 and 2). Profile AWI-20030400 was located further north, off the Godthåb Gulf, in order to gain insight into north–south trends in the crustal structure.

In this study, we use the definition of a COT zone provided by Whitmarsh & Miles (1995): the COT is that part of the lithosphere, which includes the crust between the thinned continental crust characterized by tilted fault blocks, and the first oceanic crust formed by seafloor spreading. Because of this, the interpretation of magnetic anomalies as spreading products, or not, has strong implications for the location of the COT. We discuss the interpretation of *P*-wave velocity models in combination with magnetic data and present evidence for wide and voluminous magmatic underplating.

2 DATA ACQUISITION AND PROCESSING

Four seismic refraction profiles were shot in the area between 72°N and 76°N off East Greenland (Jokat *et al.* 2004) during cruise Arktis XIX/4 of R/V *Polarstern* in summer 2003 (Fig. 1). Two profiles were

located near the Greenland Fracture Zone and Shannon Island. The two profiles used for this study, are perfectly located for comparisons of the deep crustal structure with a former transects of this region and with the conjugate Vøring Margin. On profile AWI-20030400, seismic signals were recorded by four three-component REFTEK (REF) land stations and 29 ocean bottom instruments [15 ocean bottom hydrophones (OBH) and 14 three-component ocean bottom seismometers (OBS)]. Along profile AWI-20030500, a total of seven land stations, 16 OBH and 14 OBS were used. Land stations recorded with 100 Hz sampling rate and OBH and OBS with 200/250 Hz, respectively. The locations of the receivers are displayed in Fig. 2. The average receiver spacing was 10 km. The seismic source consisted of an array of five G-guns with a total volume of 42.5 L and an additional 32 L *Bolt* airgun fired every 60 s. The shot distance was about 125 m.

OBH 403 yielded no reliable data, while OBS 416 and REF 430 had a 1 and 2 s time shift and were used for processing after an adequate traveltimes correction. On the southern profile, REFs 535 and 534 and OBHs 526 and 520 and OBS 509 had recording problems and were not used for modelling. For *P*-wave modelling, we used hydrophone recordings of the appropriate ocean bottom instruments, as well as the recorded vertical *z*-component of the onshore receivers. Stacking the vertical component channels for each REF stations did not result in better data quality. A tapered bandpass filter of 4.5–30 Hz was used for the seismic data. All displayed seismic sections (Figs 7(a–d) and 8(a–d)) are filtered with 4.5 and 12 Hz to enhance the display quality and are scaled with an automatic gain control (AGC) window of 2 s. The reduction velocity is 8 km s^{−1}. Deconvolution filters were tested, with the intention of enhancing

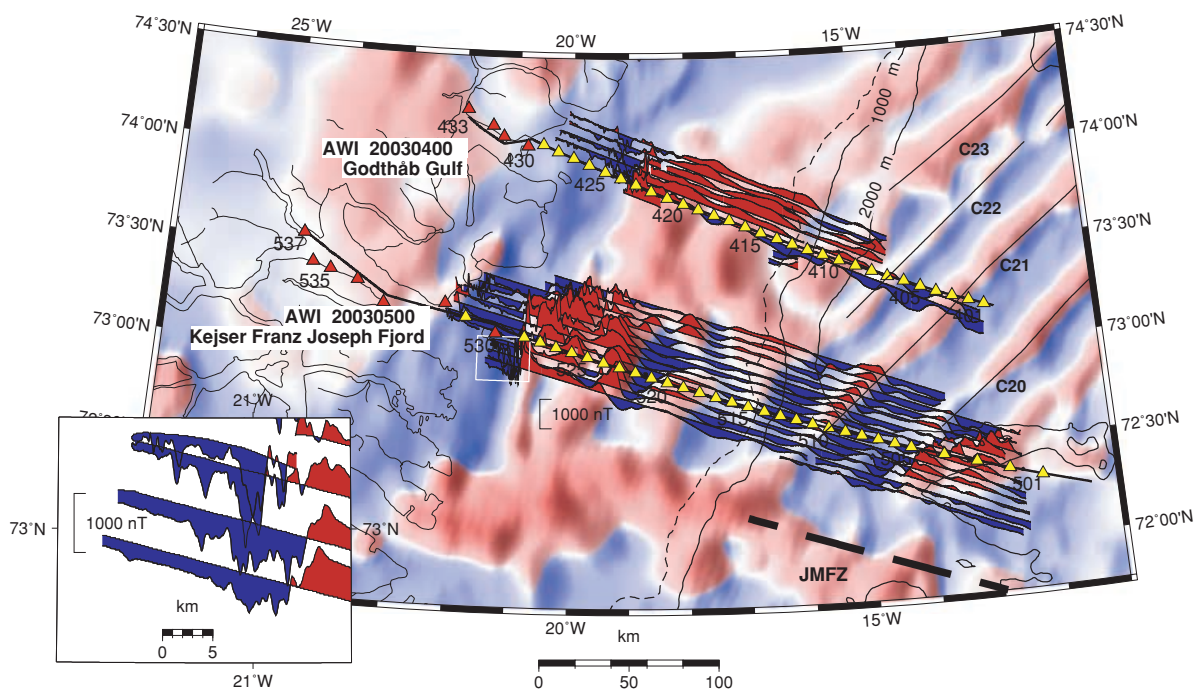


Figure 3. Wiggle plot along new magnetic survey traverse lines. See text for range of maximum values. Background shows regional magnetic grid (Verhoef *et al.* 1996). Positive values are red, negative values are blue. Seismic profiles are shown as in Fig. 2. Spreading anomalies modified after Escher & Pulvertaft (1995). White box denotes portion of map depict in inset. Note the short wavelength magnetic variations within the pronounced negative magnetic anomaly. Scale is valid for 73°N.

secondary arrivals, but did not provide significant improvements for this data set.

An aeromagnetic survey was flown using a Scintrex Caesium-vapour magnetometer sensor towed 30 m under a helicopter. The survey was flown at 100 m altitude with a line spacing of 5 km (Fig. 2). In total, 2000 km were flown in the northern part and 5500 km in the southern area. A data point spacing of 40 m results from the sampling rate of 1 Hz and an average cruising speed of 40 m s⁻¹. The magnetic data were reduced with IGRF and diurnal corrections from the *Danish Meteorological Institute* in Denmark (Fig. 1) (data available at <http://web.dmi.dk/fsweb/projects/chain/#list>). Owing to local atmospheric variations and the 300–550 km distance between the survey area and the ground station, the diurnal data were lowpass filtered at 1800 s to avoid short wavelength misscorrections. The resulting magnetic anomalies range between –1312 and 1064 nT in amplitude. After levelling, the mean cross line mistie is less than 10 nT and an absolute maximum value of 130 nT. Fig. 3 shows the new magnetic data as wiggles along the survey lines with the regional magnetic grid (Verhoef *et al.* 1996) in the background.

Gravity data were recorded continuously with a sampling rate of 10 s along the ship track for the entire cruise with an onboard fixed installed KSS 31 Bodenseewerke gravimeter. The data were converted to Bouguer anomalies and lowpass filtered at 100 s in order to reduce the high frequency noise of the ship movements. Only full circles in the ship track were cut out but other minor course variations remained and appear as small-scale variations in the profile data. The full range of the Bouguer anomaly data along the profiles used for this study is between –50 and 200 mGal.

3 MODELLING

P-wave traveltimes arrivals were picked with the *zp* software from *B.C. Zelt* (available at <http://www.soest.hawaii.edu/>

~bzelt/zp/zp.html). This programme calculated the signal to noise ratio within a 0.25 s time window before and after each pick time and associated it with an error value ranging between 0.04 and 0.15 s.

Prior to ray tracing, shots and receivers have to be in a single plane. Thus, a projection of the receiver locations onto a straight line is necessary, due to the slightly curved geometry of the transects within the fjords. A straight line fit through stations 401 and 429 was used for profile AWI-20030400 and through stations 501 and 531 for AWI-20030500 (Fig. 2). The maximum perpendicular projections onto the lines were 5.3 km for OBH 413 and 22 km for REF 537. The true offsets of the observed *P*-wave arrivals remained unchanged. This projection results in averaging of laterally inhomogeneous crustal structures due to the different ray paths between the real profile and the approximation.

Stations located onshore were projected onto the seafloor and a static correction was applied to account for the differences between rock and water sound velocities. The observed traveltimes of REF 432, 431 and 430 were corrected, assuming a vertical ray incidence, and a rock velocity of 5.2 km s⁻¹ derived from the curvature of first arrivals. The same procedure was applied to REF 536, 533, 531 and 529. The errors resulting from these approximations are estimated to be smaller than the pick uncertainties. Traveltimes arrivals for REFs 433 and 537 were located at the origin of the projection lines and no projection onto the seafloor was necessary.

The *P*-wave velocity models were obtained by forward modelling with two-dimensional (2-D) ray tracing software *RAYINV* (Zelt & Smith 1992). 2-D inversion was also used in questionable areas of the model, in order to obtain further modelling ideas. The formal error analysis for the individual phases is summarized in Table 1. The normalized χ^2 value is based on the assigned error value of each pick. Initial values for layer velocities were determined from the slopes of the traveltimes curves. After this, we focused on

Table 1. Number of used observations (n), rms misfit between calculated and observed picked traveltimes (t_{rms}) in seconds and normalized χ for individual phases of each profile. See Table 2 for phase nomenclature.

Phase	20030400			20030500		
	n	t_{rms} (s)	χ	n	t_{rms} (s)	χ
Pw	560	0.208	8.687	255	0.186	8.294
Pg1*	—	—	—	10	0.057	1.21
P1P	—	—	—	19	0.257	3.096
Pg1	426	0.123	3.703	156	0.118	4.843
P2P	134	0.161	2.783	24	0.096	1.059
Pg2	190	0.092	2.709	373	0.105	3.363
P3P	—	—	—	25	0.05	0.232
Pg3	1194	0.082	1.672	877	0.119	2.48
Pc1P	36	0.098	1.538	11	0.168	3.227
Pc1P'	20	0.118	2.073	—	—	—
Pc1	1980	0.107	1.394	1940	0.13	2.003
Pc2P	569	0.145	2.466	611	0.183	2.896
Pc2P'	56	0.214	2.942	—	—	—
Pc2	768	0.181	4.903	85	0.316	14.112
PmP	658	0.153	2.049	169	0.25	6.714
PmP'	211	0.185	2.114	24	0.124	0.88
Pn	140	0.112	1.379	53	0.136	4.063
Pn'	—	—	—	230	0.97	0.957
All	6942	0.137	2.804	4862	0.147	3.049

fitting the slope of the first arrivals rather than minimizing residuals (Figs 4 and 5). This results in individual cases in large normalized χ^2 values. For profile AWI-20030500 largest deviations to the optimum normalized χ^2 value of 1.0 are caused by small error values for the Pw phases or larger misfits to Pc2 picks and yield values of 8.294 and 14.112, respectively (Table 1). Highest t_{rms} values of profile AWI-20030400 occur at phases Pw and Pc1P' and of profile AWI-20030500 at Pg1*, Pc2 and Pc2P (see Table 2 for origin of phases). The total RMS misfits result in 0.137 s for profile AWI-20030400 and 0.147 s for profile AWI-20030500 and in normalized χ^2 values of 2.804 and 3.049, respectively. Fitting the curves of traveltimes arrivals for adjacent receiver stations often leads to a compromise of vertical and lateral velocity gradients. Ray paths bend more for larger velocity gradients within a layer. Therefore, in some cases, shorter maximum offsets could be modelled and rays did not reach observed picks (see Fig. 4 for OBHs 404, 418 and Fig. 5 for OBHs 504 and 506). In total, 7336 picks were used for AWI-20030400 and 5036 picks for AWI-AWI-20030500. Rays were traced for 88 and 93 per cent of the observations on the two profiles. Layer boundaries were constrained where wide-angle reflections were identified. In all other instances, the layer boundaries were shifted to adjust the velocity gradients within the layers.

Traveltimes arrivals were assigned as listed in Table 2 and correspond to the model layers as in Figs 6(a–d). P1P–P3P mark reflections on layers interpreted as sedimentary layers and/or upper oceanic layer 2; Pg1–Pg3 correspond to refracted rays. Pc1P and Pc2P were used for reflections at the continental crust and lower oceanic crustal layers. PmP stands for Moho reflections. The corresponding refracted rays are labelled as Pc1, Pc2 and Pn for the mantle. An additional thin top sedimentary layer was obtained from MCS data (AWI unpublished data, see Jokat *et al.* (2004) as reference) in the oceanic part of profile AWI-AWI-20030500. Only two P1P reflections on OBH 501 and 502 and Pg1 refractions from OBH 507 (Fig. 5) provided constraints on this layer. For the interpretation, the layer was not distinguished from the one beneath. Some traveltimes arrivals (Pc1P', Pc2P' and PmP') were identified with a multiple reflection within the water column. Examples are shown in Figs 7(a)

and 8(a). Pn' arrivals were modelled as head waves propagating along the Moho but with the P -wave velocity of the upper mantle (Fig. 5, e.g. 501–505).

The coverage of refracted and reflected rays traced for each layer (Figs 6a–d) gives an impression of the reliability of the models. The calculation of the model resolution is strongly dependant on the parametrization of the velocity–depth model. Only a uniform spacing of nodes would be meaningful, which was not practicable in this case. Instead, the model uncertainties were estimated by the perturbation of single node parameters until the fit of calculated traveltimes was no longer acceptable. Errors for the seismic velocities are hereby estimated as ranging from $\pm 0.1 \text{ km s}^{-1}$ for upper sedimentary layers to $\pm 0.2 \text{ km s}^{-1}$ for the lower crustal layers. The resulting uncertainties in the modelled depths of layer boundaries vary between ± 0.2 and 0.5 km for the upper layers and $\pm 2.0 \text{ km}$ for the lower ones, depending on the coverage of reflected rays. These uncertainties have to be considered as rough estimates since the perturbation could not be performed for all nodes.

4 RESULTS

We present the results of P -wave velocity modelling across the East Greenland margin for the Godthåb Gulf profile AWI-20030400 and Keiser Franz Joseph Fjord profile AWI-20030500 separately. Figs 4 and 5 show the picked traveltimes arrivals of all stations and examples of data are shown in Figs 7(a–d) and 8(a–d), which are representative for the data quality. Velocity models are shown in Figs 9 and 10.

A rough separation into three distinct crustal units simplifies the description of the velocity models; continental crust, transitional crust and oceanic crust. The structural interpretation will demonstrate that the transitional crustal unit correlates with the tectonic and magmatic definitions of a COT zone.

To distinguish the different oceanic crustal layers, we use the classification of White *et al.* (1992) for mean oceanic crustal structures. Oceanic layer 2 ($2.5\text{--}6.6 \text{ km s}^{-1}$) consists of extrusive basalts. Oceanic layer 3 ($6.6\text{--}7.6 \text{ km s}^{-1}$) is generally presumed to be of gabbroic material. Some authors use more subdivisions of the oceanic layers (Fowler 2005; Mjelde *et al.* 2005) and distinguish between layers 2A and 2B of pillow lavas and sheeted dikes. Divisions into layers 3A and 3B distinguish between gabbros ($6.6\text{--}6.9 \text{ km s}^{-1}$) and more cumulate-rich gabbros ($7.2\text{--}7.7 \text{ km s}^{-1}$).

4.1 The Godthåb Gulf profile (GG) AWI-20030400

Profile AWI-20030400 (Fig. 2) has a total length of 320 km. Four stations were deployed onshore and recorded seismic signals up to 220 km distance. OBH/OBS instruments recorded diving and reflection waves at a maximum offset of 180 km, and a mean of 115 km. The corresponding P -wave velocity model is shown in Fig. 9.

4.1.1 Continental crust (km 0–100)

The western part of the seismic profile between km 0 and 100 shows an almost 30 km thick continental crust. The westernmost land stations, REF 433–430, are located on Carboniferous sediments on Clavering Ø (Escher & Pulvertaft 1995). Signals from a 1 km deep sedimentary basin with a velocity of 4 km s^{-1} can be detected on the first 15 km of the profile. Two additional basins, each with a width of 10 km and velocities between 3.4 and 3.7 km s^{-1} , can be modelled from stations 429, 428, 426 and 425. The depths of the basins are assumed to be less than 1 km. Velocities in the continental sediments

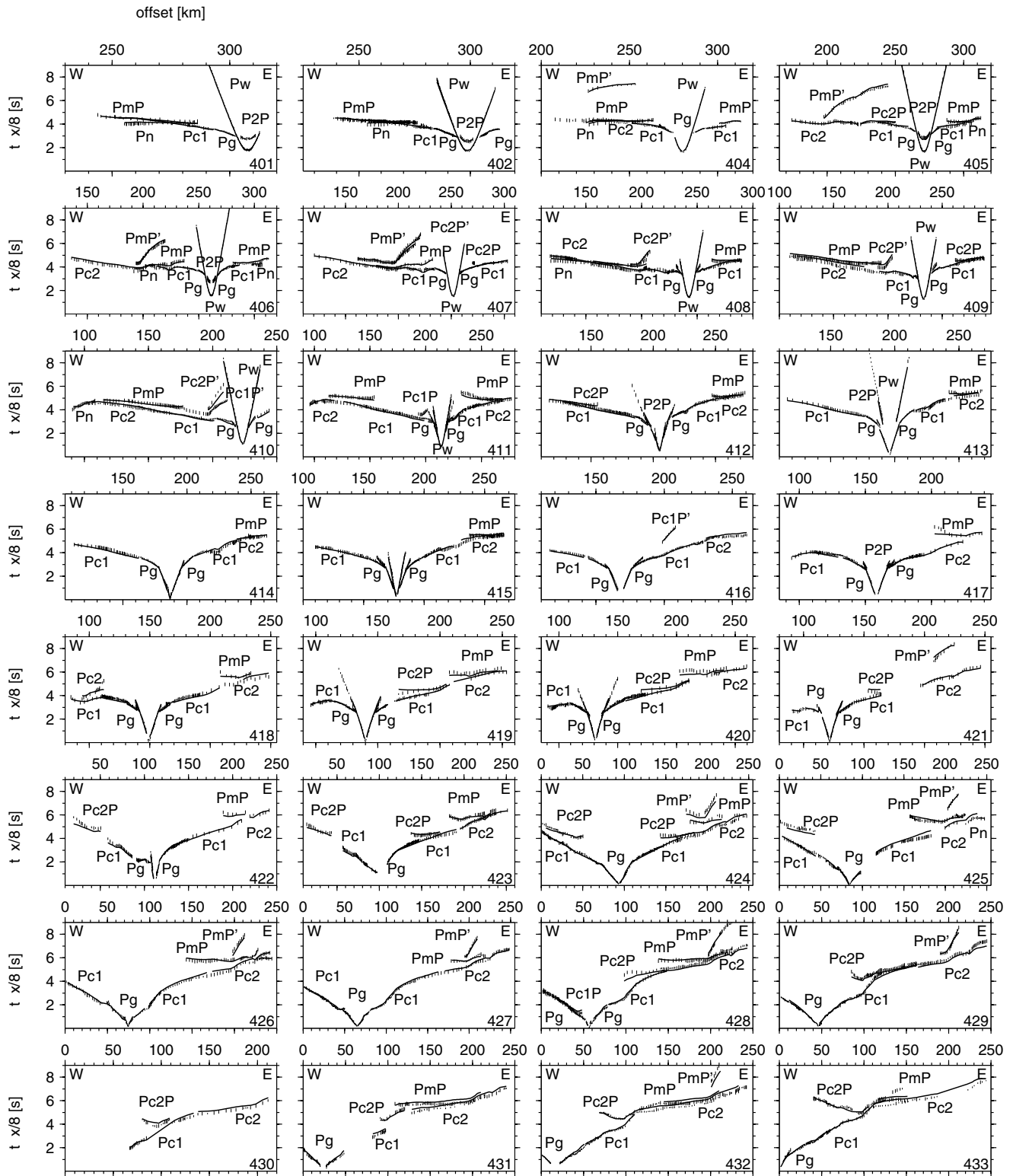


Figure 4. Observed and calculated *P*-wave arrivals for profile AW1-20030400. Observed arrivals are assigned with a vertical error bar. The picked arrival time is in the centre. Lines show the calculated arrivals. Note the variety of *PmP'* and *Pc2P'* phases. See Table 2 for nomenclature of phases. Short offset phases are not differentiated and labelled as *Pg*.

increase rapidly from 4.8–5.2 km s⁻¹ near the surface to 5.9–6.1 km s⁻¹ at 5 km depth (0.13–0.25 km s⁻¹ km⁻¹). A single reflection at the bottom of this layer is modelled from station 428 (Figs 4 and 6a). A low gradient (0.03–0.05 km s⁻¹ km⁻¹) crystalline continental

crust is well constrained by *Pc1* phases with *P*-wave velocities of 6.0–6.1 km s⁻¹ at 5 km depth and 6.9–7.0 km s⁻¹ at the bottom. These latter values are slightly higher than the global average for continental crust (Christensen & Mooney 1995). The layer boundary

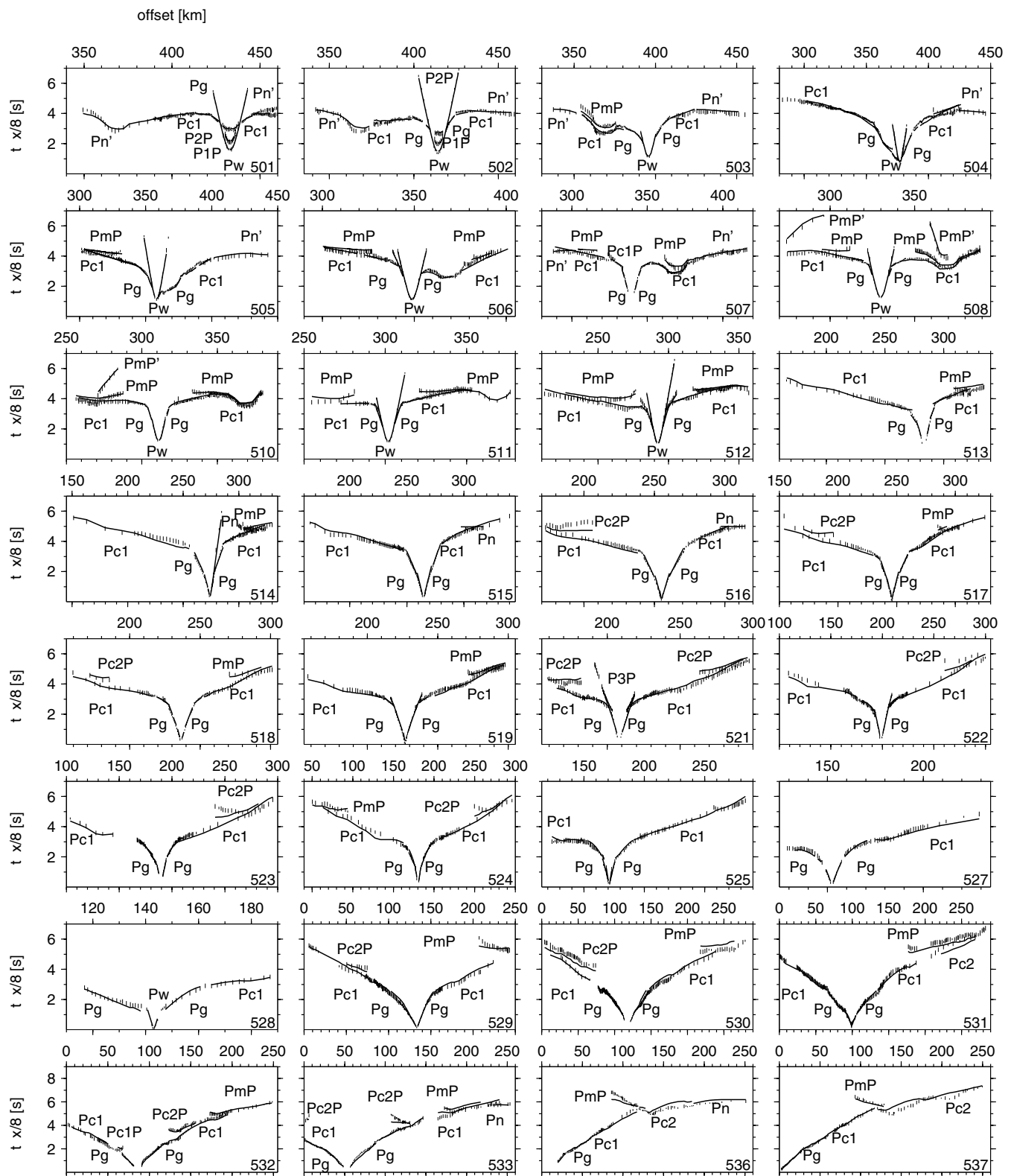


Figure 5. Observed and calculated *P*-wave arrivals for profile AWI-20030500. See Fig. 4 and Table 2 for explanations.

at 5 km depth represents a change in seismic gradient and is not connected with an impedance contrast. A basement high at km 100 is clearly resolved from several stations (Fig. 4). A significant delay of *Pc1* traveltimes arrivals is observed eastward of the escarpment.

The different *Pg3* slopes of OBH 424 east and 423 west confirm the modelled basement high at this part of the profile. *Pc2P* phases infer a reflector in the lower continental crust, rising up from km 20 in 29 km depths to 18 km depth at km 100 (Fig. 6a), which represents

Table 2. Nomenclature of seismic phases.

Layer of velocity models	rfl on top of layer	rfr in layer
Layer 1 : upper sediments (1 & 1* of AWI-20030500)	Pw P1P	Pg1 Pg1, Pg1*
Layer 2: intermediate layer	P2P	Pg2
Layer 3: lower sediments	P3P	Pg3
Layer 4: upper crust	Pc1P, Pc1P'	Pc1
Layer 5: lower crust	Pc2P, Pc2P'	Pc2
Layer 6: upper mantle	PmP, PmP'	Pn, Pn'

Notes: rfl, reflection; rfr, refraction. Pw phase reflects at seafloor. An additional thin layer was inserted at the top for model AWI-20030500. Reflections on this layer are labelled with P1P, a refraction phase with Pg1*. Phase Pc1P', Pc2P', and PmP' have a multiple reflection between the water surface from below and the seafloor. Pn' represents head waves along the Moho.

a significant velocity contrast. Beneath this lower crustal reflector, a clear and almost continuously resolved reflector was modelled from PmP arrivals. The lower crust is modelled with velocities of 7.2–7.4 km s⁻¹ between the two prominent reflections.

4.1.2 Continent–ocean transition zone (100–224 km)

The transitional crustal unit extends from km 100 to 224. Landwards, it is bounded by the continental basement high. A shallow, most probably volcanic, basement high and the first clearly identifiable magnetic spreading anomaly, C22, marks the transition into oceanic crust in the east (Fig. 9). The upper sediment layer on the shelf has a thickness of ~2.5 km (2.0–2.8 km s⁻¹). Secondary Pg2 arrivals at OBH 422 and 419–415 yield a thin (<500 m) intermediate layer (~4.1 km s⁻¹) beneath. Only sparse reflections sample the top of this thin layer, which terminates seaward in the shallow feature interpreted as of volcanic origin (Pg2 arrivals of OBH 411–410) at km 224 (Figs 4 and 6b). Three crustal layers of the transition zone can be distinguished on the basis of their different velocity gradients. The upper part has a velocity gradient of 0.35–0.47 km s⁻¹ km⁻¹ with velocities between 4.6–5.5 km s⁻¹ at 3 km depth and 5.8–6.5 km s⁻¹ at 7 km depth. Two Pc1P' (Table 2) reflections constrained the boundary between km 205 and 220. In the middle part, an increasing velocity gradient of 0.04–0.1 km s⁻¹ km⁻¹ is modelled from west to east. Seismic velocities range between 6.4–6.8 km s⁻¹ at 7 km depth and 6.8–7.1 km s⁻¹ at 13–17 km depth. Diving waves penetrate almost 2/3 of the crustal layer, and have their deepest turning points at 9–12 km depth (Fig. 6b). Several Pc2P and Pc2P' (Table 2) reflections (Figs 4 and 6a) were modelled, constraining the intracrustal and seaward rising reflector. The significant velocity contrast along this reflector, as modelled in the continental part of the profile, becomes less prominent to the east. A high velocity lower crustal layer (7.15–7.4 km s⁻¹) yields a very low velocity gradient of 0.01 km s⁻¹ km⁻¹. PmP and PmP' resolved the Moho along the entire transition zone. The maximum thickness of the high velocity layer is 16 km at a depression in the Moho near km 124. Upper mantle velocities of 8.0 km s⁻¹ were derived from Pn arrivals (Figs 4 and 6a) between km 140 and 250.

4.1.3 Oceanic crust (224–320 km)

The eastern crustal unit of the profile has the characteristics of typical oceanic crust (White *et al.* 1992), consistent with the presence of the first clearly identified magnetic spreading anomaly, C22, near km 250/OBH 407. An upper sedimentary layer was modelled with

velocities in the range 1.6–1.9 km s⁻¹ and thickness decreasing seawards from 1.25 to 0.75 km. A basal reflector is inferred for this unit from four P2P arrivals (Figs 6a and 9). Upper oceanic crust was modelled to consist of two layers with different velocity gradients. The upper layer has velocities of 3.2–5.0 km s⁻¹, the lower one velocities 4.6–6.0 km s⁻¹, which is well defined by Pg3 arrivals (Fig. 6b). At the eastern end of the profile, between km 280 and 320, MCS data show rough topography (AWI unpublished data; see Jokat *et al.* (2004) as reference). A lower 4–5 km thick oceanic layer was modelled, with *P*-wave velocities of 6.6–6.7 km s⁻¹ at the top and 6.9–7.0 km s⁻¹ at the base. The velocity gradient of the lower layer falls in the range for standard lower oceanic layers (White *et al.* 1992). Pc1P arrivals at OBHs 402–409 resolved a distinct reflector in the oceanic crustal part of the profile. Beneath this, thickened oceanic crust was modelled from Pc2 arrivals with velocities of 7.2–7.4 km s⁻¹. PmP and PmP' arrivals (Fig. 6a) resolved the Moho in 10.1–15.8 km depth, and show a decrease in total thickness of the oceanic crust from 13.7 to 6.8 km between km 224 and 300. An upper mantle velocity of 8.0 km s⁻¹ was modelled from several observed Pn arrivals.

4.2 The Kejser Franz Joseph Fjord profile (KFJF) AWI-20030500

Profile AWI-20030500 has a total length of 460 km. Seven land stations recorded seismic signals at distances of up to 250 km. OBHs and OBSs recorded arrivals of refraction and reflection waves out to an average distance of 80 km with a maximum of 170 km. This profile overlaps with profile 94320 (Schlindwein & Jokat 1999) for a distance of almost 120 km (Fig. 2). The overlapping part of the crustal transect was used as a starting model for the continental part of profile AWI-20030500. Only minor adjustments were necessary due to the different orientations of both transects. In the eastern, oceanic, part, between km 280 and 460, horizons of the two top sedimentary layers were digitized from time migrated multichannel seismic data (AWI unpublished data; see Jokat *et al.* (2004) as reference).

Fig. 10 shows the corresponding *P*-wave velocity model. The following description of the results is organised as for profile AWI-20030400.

4.2.1 Continental crust (0–130 km)

The top continental sediment layer (5.2–6.0 km s⁻¹) reveals average velocity gradients of 0.13 km s⁻¹ km⁻¹. A 1.5 km—deep basin is imaged by short offset arrivals (3.6–5.0 km s⁻¹) (Fig. 5, OBH 531) west of Bontekoe Ø (km 85–125). The top velocities decrease to 3.2 km s⁻¹ beneath the outcrop of plateau basalts (Escher & Pulvertaft 1995). Between km 0 and 70, upper crustal velocities (6.1–6.5 km s⁻¹) fall within the global average range of velocities for continental crust (Christensen & Mooney 1995). Further east, the values increase constantly (Fig. 10) and the velocity gradient increases from 0.02 to 0.05 km s⁻¹ km⁻¹. Pc2P and PmP reflections revealed a west dipping mid-crustal reflector at 17–20 km depth and a similar—dipping Moho at 27–31 km depth between km 50 and 100 (Figs 6 and 10). A Moho plateau is modelled at 26 km depth from further PmP reflections (Fig. 5 REF 533, 532 and OBH 524). The strong horizontal velocity increase in the lower crustal layer near km 50 (Fig. 10) was adopted from profile 94320 (Schlindwein & Jokat 1999). Similar velocities of 6.8–7.2 km s⁻¹ were calculated from Pc2 arrivals but the modelling of this phase revealed major misfits

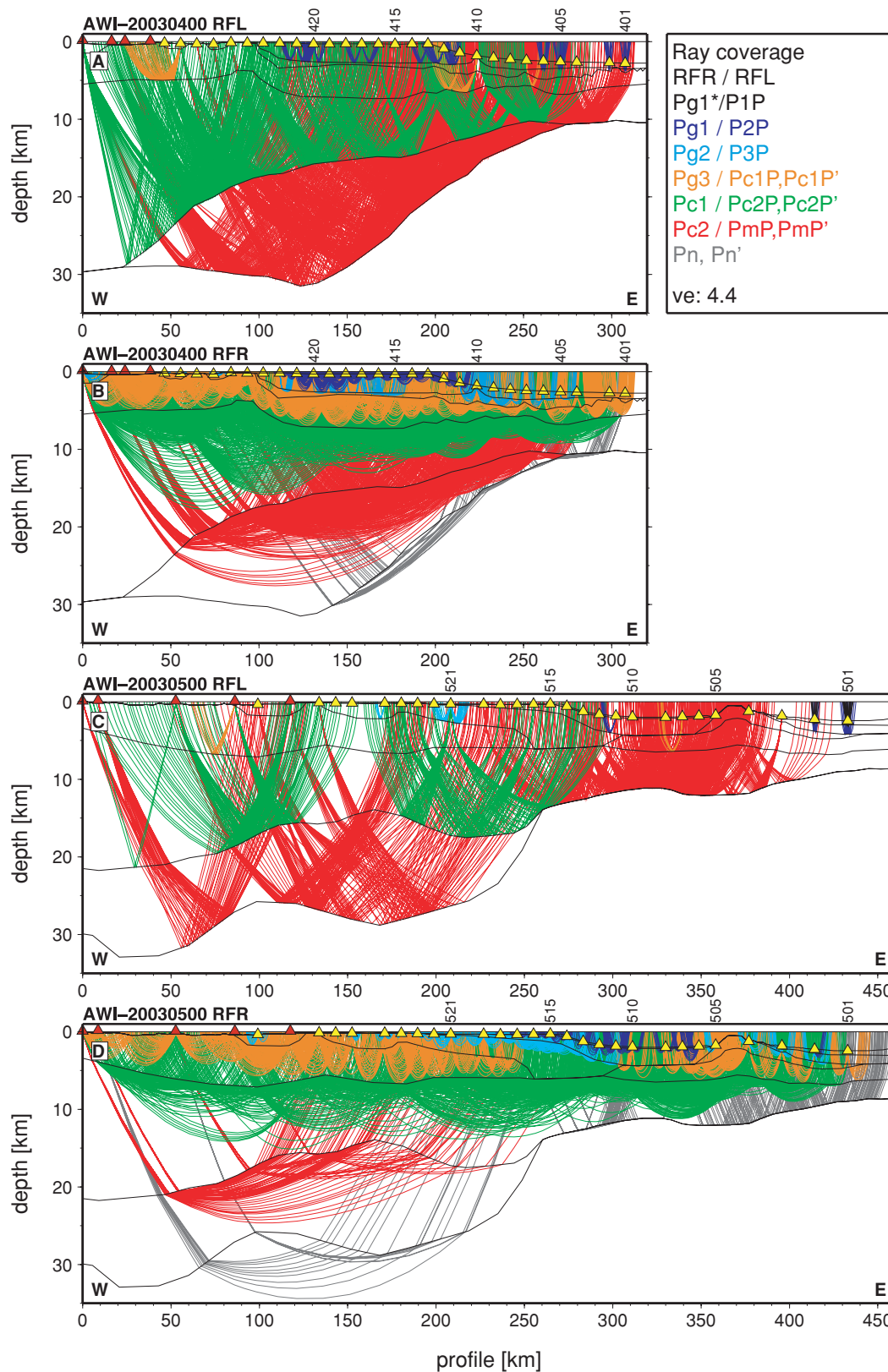


Figure 6. Ray tracing for both profiles. RFL: reflected rays. RFR: refracted rays. Vertical exaggeration is 4.4. Triangles represent receiver station locations as in Fig. 2. The different colours symbolize the rays for the individual layers. See Table 2 for a further explanation of the phases. (A) All reflected rays for profile AWI-20030400. Note the excellent coverage of the intra crustal reflector and the Moho by Pc2P and PmP phases. From km 270 on Pc2P phases equal PmP phases. (B) All refracted rays for profile AWI-20030400. Only individual Pn phases traced the upper mantle. (C) All reflected rays for profile AWI-20030500. From km 260 on Pc2P equal PmP phases. (D) All refracted rays for AWI-20030500. See text for model parameters and velocities.

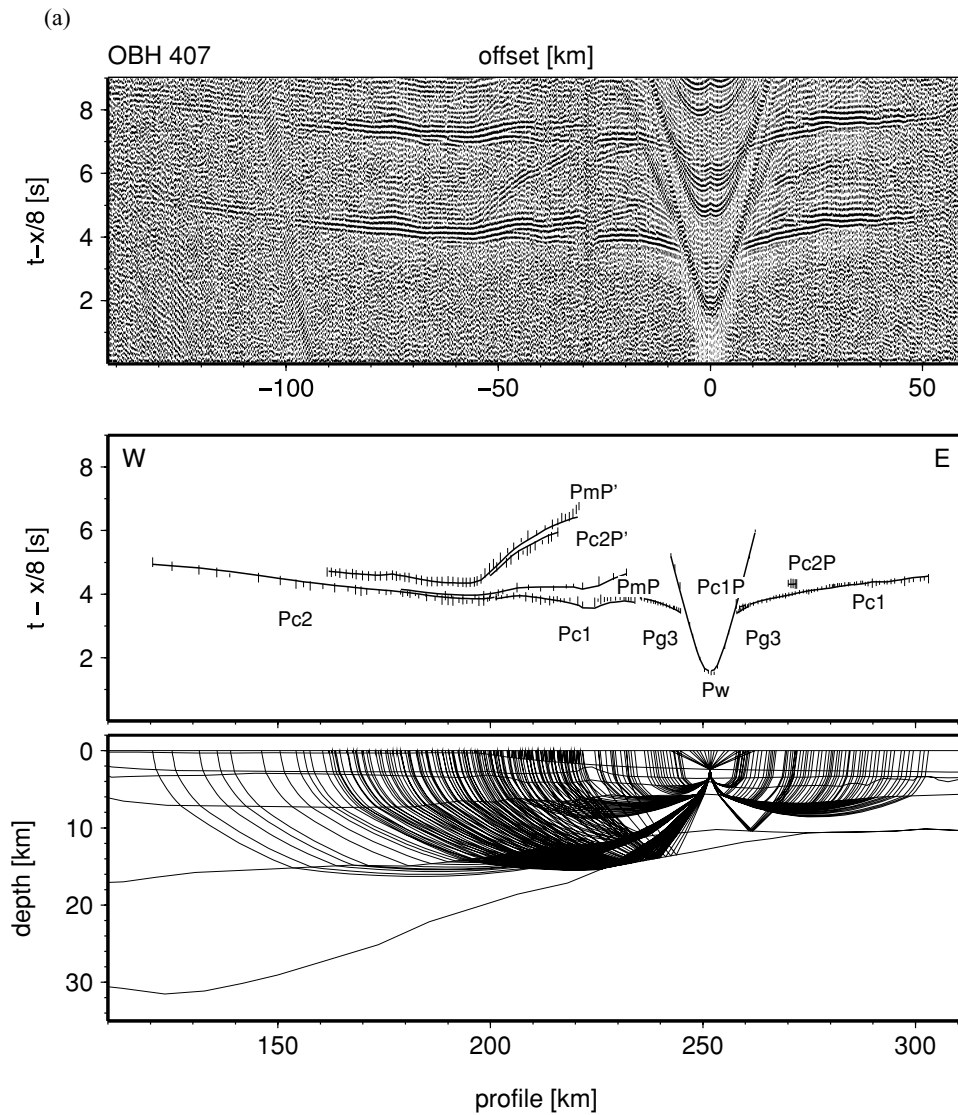


Figure 7. Examples of recorded seismic data from profile AWI-20030400. A 4.5–12 Hz bandpass filter was applied. The signals are scaled by automatic gain control in windows of 2 s. The traveltimes are reduced by 8 km s^{-1} . Observed phases are labelled (see Table 2). The ray coverage of each station is marked in the lower model. (a) Station 407 represents recordings of the oceanic crust and the eastern COT. Note the multiple reflected phase PmP' and $\text{Pc2P}'$. (b) Station 415 is placed within the COT and shows typical shorter offsets. (c) OBH 423 is located near the landward termination of the COT. (d) Land station 431 shows typical long offsets. Note the poor quality of data between km 150 and 250. A filter of 4.5–21 Hz was here applied. The offset between the first arrivals and the location is due to the horizontal deviation of the station to the ship track.

(Fig. 5 REF 537). Besides the Moho plateau, all crustal velocities and layer boundaries are in good agreement with the overlapping part of profile 94320.

4.2.2 Continent–ocean transition zone (130–260 km)

This 130 km long part of the model represents an area of increased crustal velocities compared to the continental crustal unit. Pg3 phases at OBH 529–527 witness the dip of the continental sedimentary layer landward of km 130 with velocities of $4.5\text{--}6.1 \text{ km s}^{-1}$ and the onset of another layer seaward of this point with velocities of $2.0\text{--}3.3 \text{ km s}^{-1}$ (Figs 5 and 10). The uppermost sedimentary layer ($2.0\text{--}2.4 \text{ km s}^{-1}$) pinches out to the west (km 210), and merges with a sedimentary basin in the oceanic crustal unit. A second dipping sedimentary layer is modelled with a strong velocity increase ($2.0\text{--}3.3 \text{ km s}^{-1}$) between km 130 and 230 and

a lower velocity range ($2.5\text{--}4.2 \text{ km s}^{-1}$) further seaward between km 230 and 260. This layer also forms a deep basin in the oceanic crustal unit (Fig. 10). The intrasedimentary layer boundaries were inferred from unpublished MCS data, but could not be confirmed by reflected P2P arrivals. Beneath, a layer extends and thins out from km 130 to 255, but with velocities ranging between 3.8 and 6.5 km s^{-1} from top to bottom. Pg3 traveltimes arrivals (Fig. 6d) yield an increase in the velocity gradient for this layer from an average of $0.13 \text{ km s}^{-1} \text{ km}^{-1}$ in the continental crust (see above) to an average of $0.55 \text{ km s}^{-1} \text{ km}^{-1}$ in the transitional unit. The top of the crystalline crust is not resolved by any Pc1P phases but most traveltimes curves show a variation of the velocity gradient at a mean depth of $6.3 \pm 0.5 \text{ km}$. Thus, within the upper-crustal layer, velocities vary in the range $6.5\text{--}6.7 \text{ km s}^{-1}$ at the top and $6.9\text{--}7.0 \text{ km s}^{-1}$ at the bottom. Between km 180 and 255, Pc2P reflections trace a pronounced bowl shaped reflector. This reflector marks

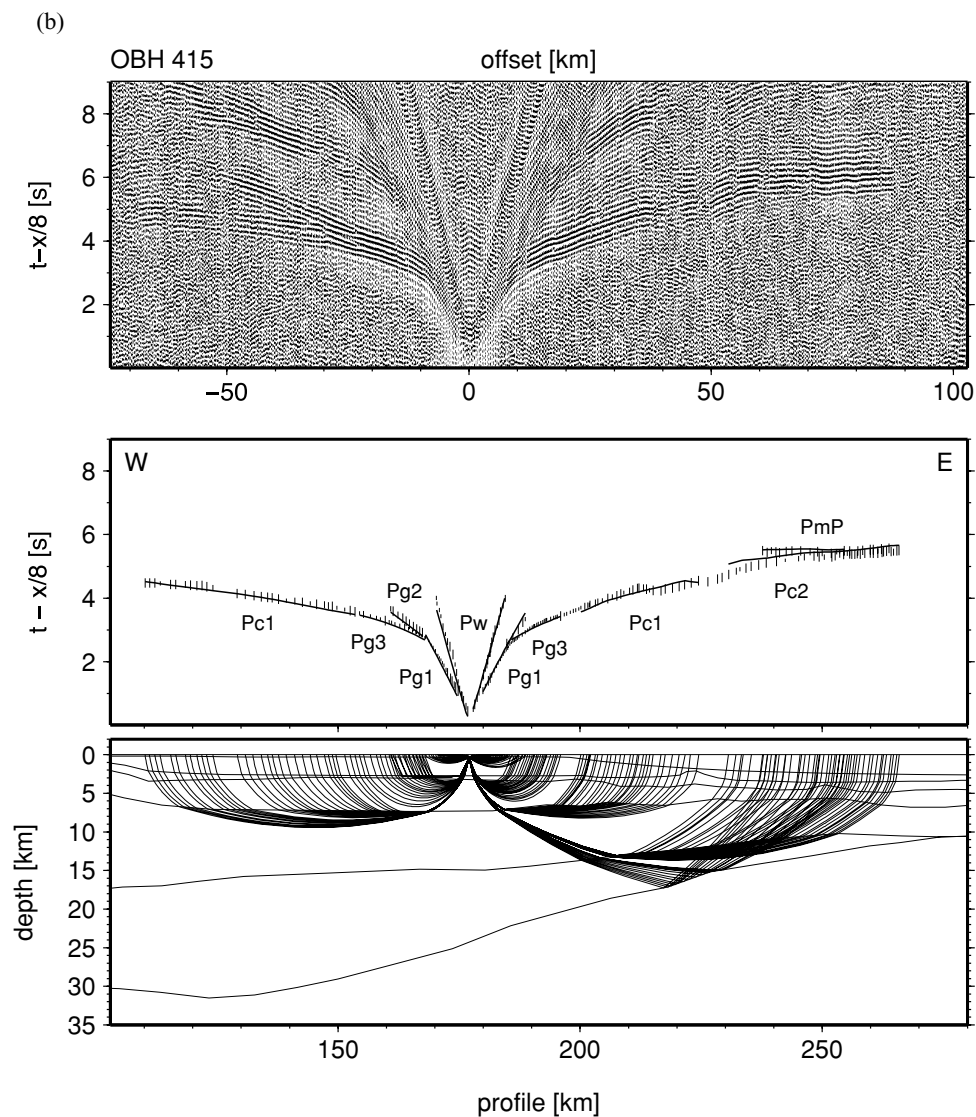


Figure 7. (Continued.)

a velocity contrast from 6.9 to 7.2 km s⁻¹. Thus, the velocity gradient within the upper crust increases marginally by up to 0.08 km s⁻¹ km⁻¹ from west to east, as is seen on profile AWI-20030400. Pc2P and PmP reflections constrain the topography of the intermittent reflector and the Moho (Figs 6 and 10). Between km 130 and 218 a Moho depression is modelled with a maximum depth of 28.8 km. The resulting maximum thickness of the high velocity layer is 15 km, near km 165. Land stations REF 537, 536, 533 and OBH 531, recorded Pc2 phases at offsets of 100–240 km (Fig. 5). Rough calculations of the traveltime arrivals yield velocities between 7.2 and 7.4 km s⁻¹, but the upper crustal topography could not be resolved by Pc2 traveltime fits without giving rise to large misfits of up to 300 ms (Fig. 5, REF 537, 536, 533 and OBH 531). The Moho slope between km 218 and 260 is not traced by any rays.

4.2.3 Oceanic crust (260–460 km)

The southeastern area of the profile, between km 290 and 460, shows typical oceanic crustal layering and velocities (White *et al.* 1992), correlating with the first clearly identified magnetic spread-

ing anomalies C21 (Escher & Pulvertaft 1995). The dipping sedimentary layer from the transitional unit forms a 30 km wide basin (3.2–4.2 km s⁻¹) between km 260 and 290. Between km 360 and 380 a ridge domes up to separate two different sedimentary basins (Fig. 10). Reflecting horizons for the two top sedimentary layers were picked from MCS data. In the west, between the shelf edge and the ridge (km 290–350), the basin fill consists of a thin (100 m) upper layer (1.9–2.0 km s⁻¹) and the layer extending from the transitional unit (2.1–3.0 km s⁻¹) (Fig. 10). The maximum thickness is 1.8 km. A thin (750 m) upper layer (1.6–1.9 km s⁻¹) and a second thin (1 km, 2.5–3.2 km s⁻¹) sedimentary layer were inserted into the model east of the ridge. Observed P1P and P2P arrivals from OBS 501 and 502 (Fig. 6c) confirm the horizons. The upper part of the ridge is modelled between km 350 and 430, with velocities of 3.0–4.0 km s⁻¹ increasing from west to east. These values are derived from Pg2 arrivals at OBHs 502–505. Beneath this, *P*-wave velocities strongly increase between km 290 and 460, from 4.5 to 6.3 km s⁻¹ down to ~6.5 km depth. In the lower oceanic crust, velocities range between 6.6 and 7.0 km s⁻¹ within a 2.5–4 km thick layer (Fig. 10). The Moho depth was constrained to 11–14 km between km 260 and 330 by Pn arrivals from stations 514 to 516

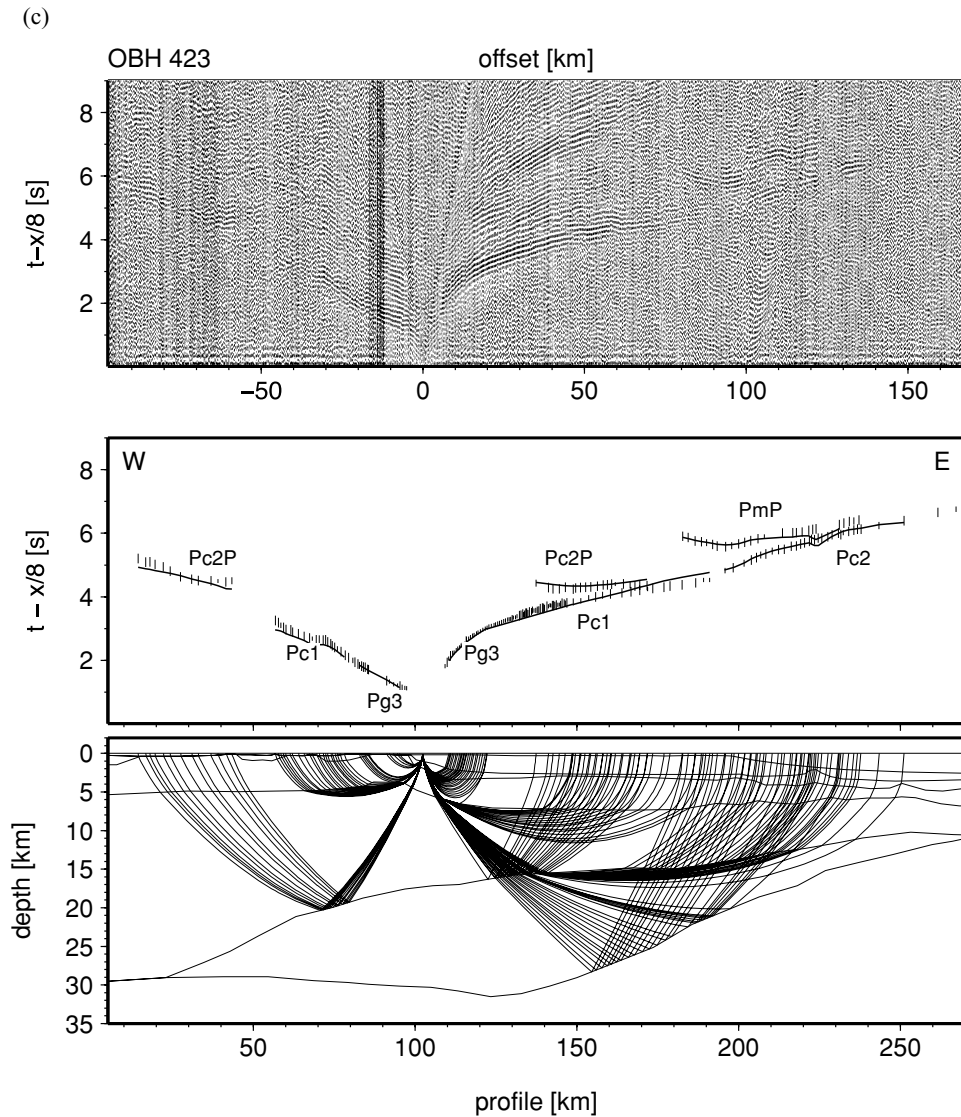


Figure 7. (Continued.)

(Figs 5 and 6d) and PmP arrivals from stations 511, 512 and 517–519 (Figs 7 and 8c). Further east, the Moho decreases to 8.6 km depth with a small root (12 km depth) beneath the ridge. The location of the Moho is based on numerous PmP, PmP', Pn and Pn' arrivals (Figs 8c and d). Traveltime arrivals of OBS 501–505 and 507 associated as mantle phases were assumed to be critically refracted and travelling as head waves along the Moho and with the upper mantle acoustic velocity of 8.0 km s^{-1} (Figs 6c and 10). The oceanic crustal thickness decreases from west to east, from 7.0 to 4.8 km. However, the maximum thickness of the ridge in the oceanic crust reaches 11.5 km.

4.3 Gravity models

2-D gravity modelling was performed for both transects to verify the consistency of the *P*-wave velocity models with the observed Bouguer anomalies. An initial density model was derived from conversion of all *P*-wave velocity nodes to density using a Nafe and Drake curve (Nafe & Drake 1957) approximation after Ludwig *et al.* (1970). Velocity layers were partly split into separate polygons with

different densities where appropriate, but each polygon was assigned with a constant density value. Adjustments to the mantle density were necessary in order to fit the gentle rise of the observed gravity data towards the oceanic part of the models. Thus, the subcontinental mantle was set to 3.31 g cm^{-3} and beneath the oceanic crust to $3.24\text{--}3.26 \text{ g cm}^{-3}$. The first approximation with a constant density of 3.05 g cm^{-3} for the lower crustal layer caused also a major misfit. A constant density of 3.15 g cm^{-3} provided a better fit. Minor adjustments were applied to the upper and middle crustal layers to obtain an even closer fit of the calculated and measured gravity anomalies. The final gravity models yield maximum deviations (residuals) to the observed gravity anomalies of 15.4 mGal for AWI-20030400 and 19.3 mGal for AWI-20030500. Density variations larger than $\pm 0.02 \text{ g cm}^{-3}$ for sedimentary and upper crustal layers and $\pm 0.01 \text{ g cm}^{-3}$ for lower crustal layers and the mantle would yield significant misfits to the observed Bouguer anomalies. The results of the gravity modelling are shown in Figs 9 and 10. Corresponding densities for the polygons are given in g cm^{-3} . The derived *P*-wave velocity models can be verified very well with the gravity models. Oceanic mantle adjustments result from a simple

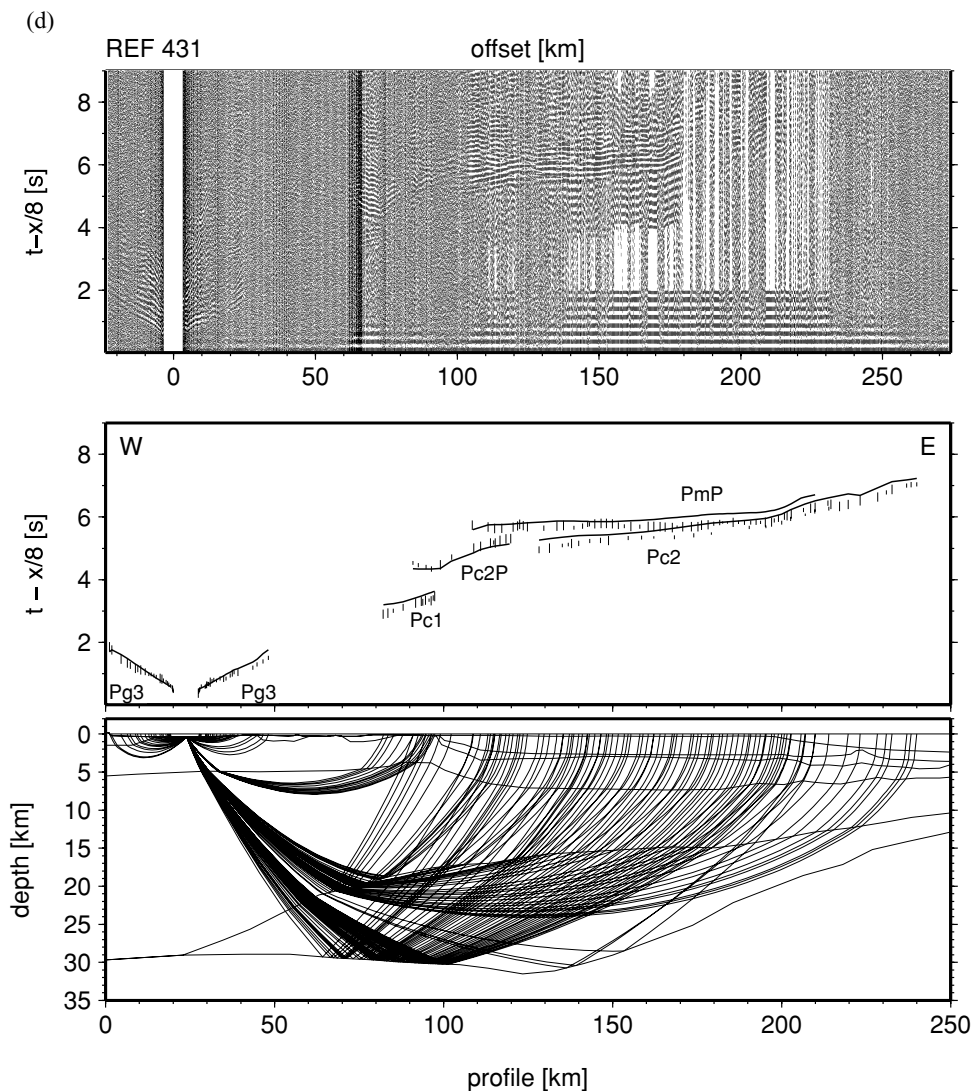


Figure 7. (Continued.)

approximation with respect to a warmer temperature compared to the subcontinental mantle and is applied commonly for volcanic rifted margins (e.g. Breivik *et al.* 1999; Schmidt-Aursch & Jokat 2005b). Three minor misfits occur at profile AWI-20030500 while the approximation for profile AWI-20030400 is excellent. In the continental part between km 0 and 140, misfits can be related to 3-D effects of intrusions and/or sediment basins, which cannot be constrained in details by the 2-D model. Misfits within the COT zone between km 200 and 290 might result also from the unresolved crust-mantle boundary between km 220 and 240 (Figs 6 and 10). The top of the ridge between km 360 and 390 was modelled with a low density of 2.1 g cm^{-3} in order to match the measured gravity values.

5 INTERPRETATION AND DISCUSSION

First-order structural interpretations derived from the P -wave velocity models and the magnetic data are presented in Figs 11 and 12. Since both velocity models are quite similar, we provide a joint interpretation of both profiles. Prominent features of each transect are outlined and discussed in detail. Fig. 13 shows an overview of the tectonic and magmatic results of the interpretations. A compar-

ison with the conjugate Vøring margin will be discussed according to the profiles shown in Fig. 14.

5.1 Continental crust

The onshore geology shown in Fig. 1 (Escher & Pulvertaft 1995) allows us to interpret Devonian to Carboniferous/Mesozoic sediments in the upper western layers of the seismic profiles (Figs 11 and 12). We have extrapolated this interpretation along the profiles, considering the P -wave velocities and the gradients, up to km 100 (Fig. 11) and km 130 (Fig. 12). However, a significant change in the velocity parameters occurs at these locations. Further eastward of them, the sedimentary layers tilt down and the velocity gradients increase. Additionally, a layer with much slower velocity (2.0 – 3.0 km s^{-1}) appears on top, which consists presumably of Cenozoic sediments (Figs 9–12). Around Bontekoe Ø (Figs 1, 2 and 12), slower velocities (3.2 – 5.0 km s^{-1}) in the 40 km wide and 1.5 km deep basin allow us to conclude the presence of volcanically intruded sediments consistent with the exposed plateau basalts on the island (Fig. 1). An equivalent interpretation for the two 0.7 km deep basins imaged on profile AWI-20030400 (Fig. 11) near km 50

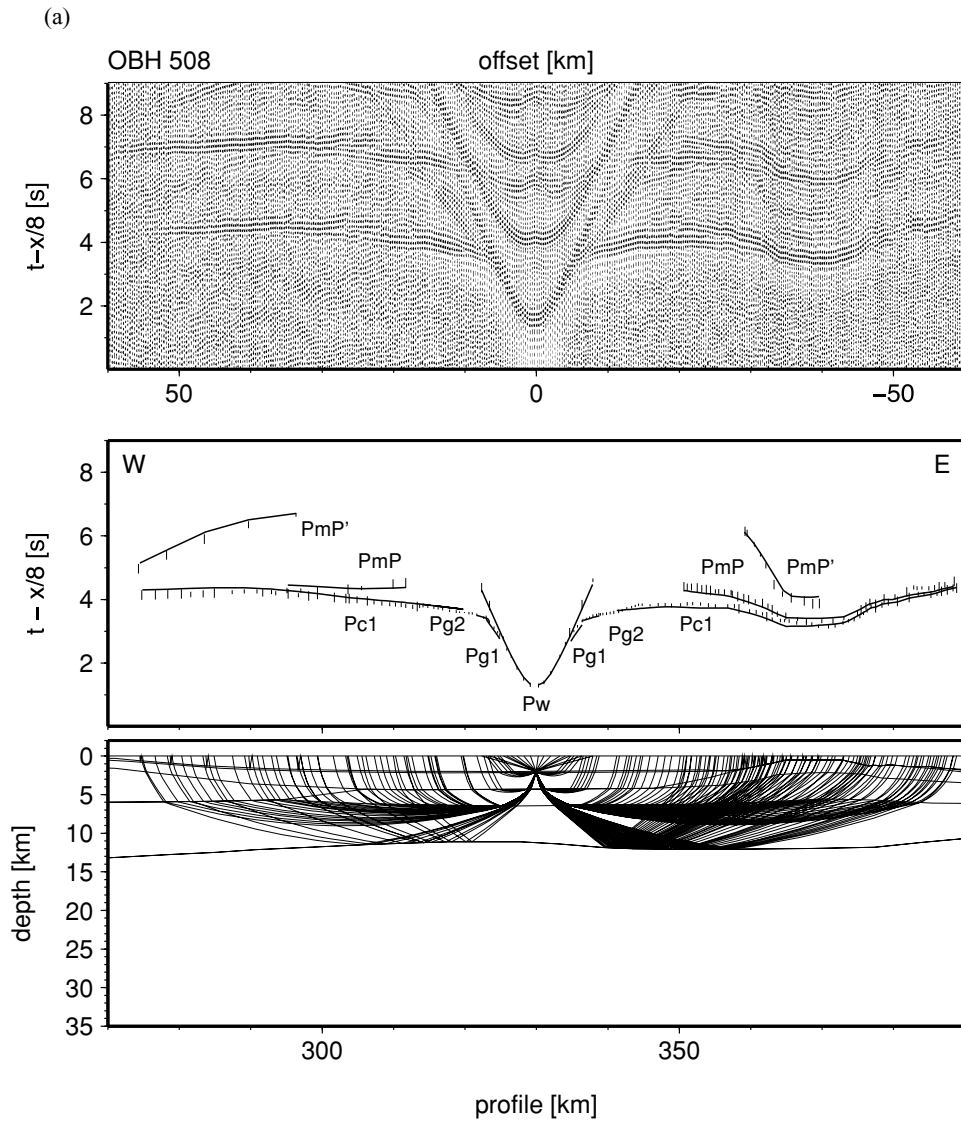


Figure 8. Examples of recorded seismic data from profile AWI-20030500. For data descriptions see Fig. 7. (a) OBH 508 represents recordings of the oceanic basin west of the ridge and the eastern COT. Note the multiple reflected phase PmP' near ± 50 km. (b) OBH 518 shows delayed arrivals due to thick Cenozoic sediments within the COT. (c) OBH 529 is located at the landward termination of the COT. (d) Continental crust, LCB and the western part of the COT are covered by station REF 536.

and 80 is most likely. The transition to the crystalline continental crust at 5–6 km depths is interpreted from the change to a lower velocity gradient (Figs 9 and 10). A Pc2P – reflector and the Moho at ~ 30 km depth is well resolved on both profiles (Figs 6a–c, 9 and 10). The westward dipping character of the reflectors was also observed on profile 94320 (Schlindwein & Jokat 1999, 2000) and attributed to Mesozoic – Tertiary extensional thinning of the continental crust from 45 to ~ 22 km. Those authors concluded that large-scale intrusions (Escher & Pulvertaft 1995) in the Mesozoic sedimentary basins and the formation of a magmatic underplate at the base of the continental crust are both consequences of a Tertiary magmatic event. Short wavelength magnetic variations (Figs 3, 11 and 12) that correlate with the area of increasing seismic velocities in the continental crust support this interpretation. A high velocity lower crust is also observed, and its further extent to the east is a notable result of this study. A detailed discussion of this pronounced layer is undertaken in one of the next sections. The coincidence of the eastward lateral increase of seismic velocities, the short wavelength magnetic

anomaly pattern, and the onset of magmatic underplating is also remarkable. It indicates an eastward increasing amount of magmatic intrusions in the continental crust and its sedimentary basins during an episode of excess magmatism. We suggest the beginning of the COT occurs at this location (km 100 at AWI-20030400 and km 130 at AWI-20030500) due to major rift-related changes in the crustal structure.

5.2 The continent–ocean transition

Earlier, we adopted the definition of the COT by Whitmarsh & Miles (1995) for a rough division into the three crustal units, continental, transitional and oceanic crust. Along the two profiles, significant crustal structure variations provide additional constraints for the westward and eastward termination of the COT. The landward terminations are dominated by an increase in seismic velocities in the upper continental crust, and thickening of the lower crustal

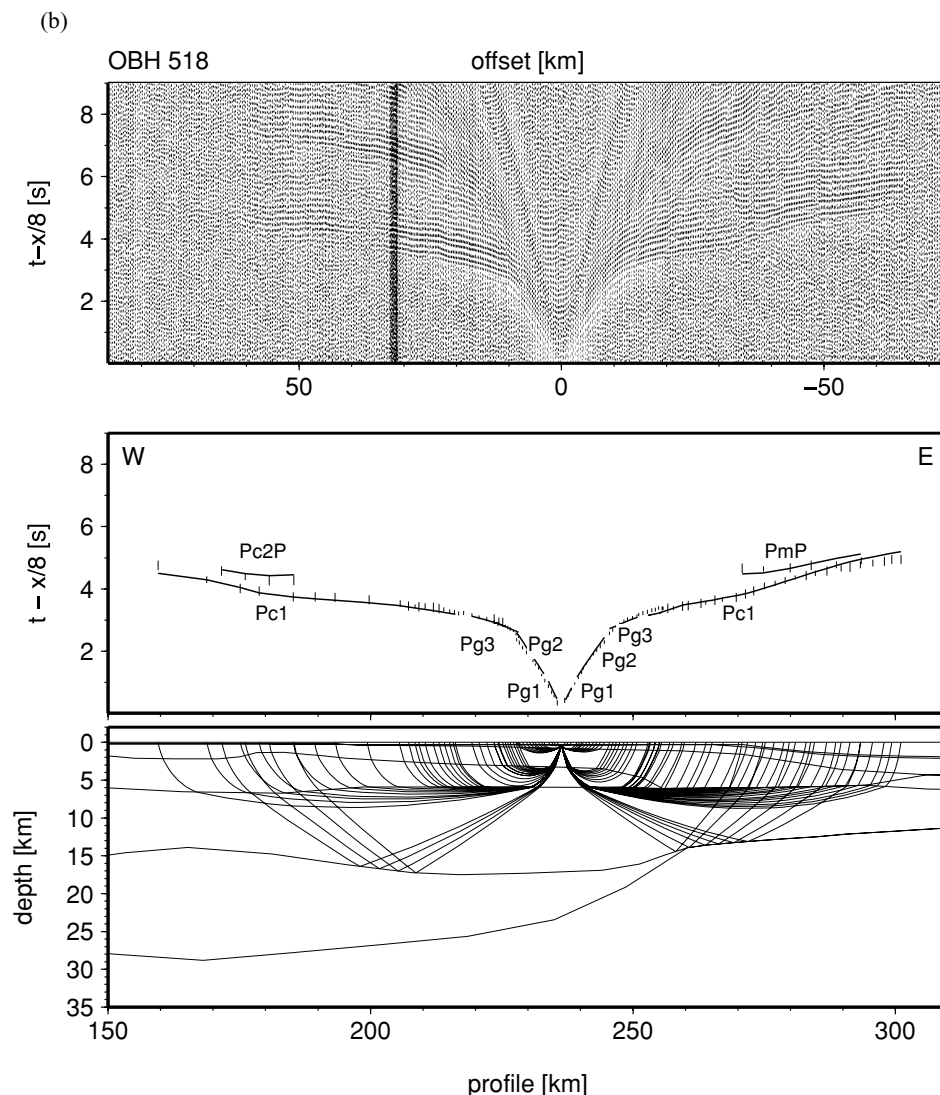


Figure 8. (Continued.)

layer (Figs 9–12). A comparison of the eastern ends of both COTs with wide-aperture CDP profiles published by Hinz *et al.* (1987) (Fig. 2) provide a pronounced correlation with their identified seaward dipping reflector sequences (SDRs).

The following interpretations describe the crustal structure of both COTs in detail.

(1) The top sedimentary layer is interpreted as Cenozoic sediments and can clearly be distinguished from the underlying layer by its much slower seismic velocities ($2.0\text{--}3.0\text{ km s}^{-1}$). We assume that the seismic velocities of $3.2\text{--}4.1\text{ km s}^{-1}$ between km 200 and 250 of profile AWI-20030400 (Fig. 9) represent an area of basalts extruded in a deep-water regime. We associate the basement high at km 225 as a volcano with increased lava flows to the west. This region correlates with the area where Hinz *et al.* (1987) identified SDRs on profile 46 (Fig. 2) westward of a basement high, which is similar to the one we found at km 225. East of that point, the crust was described as normal oceanic crust. A projection of SDRs identified on profile 46 would fall into the crustal layer beneath, between km 200 and 225 and in 3–7 km depth (Fig. 11). Hinz (1981) suggested that SDRs were erupted over highly extended continen-

tal crust prior to seafloor spreading. Thus, we suggest the seaward termination of the COT at km 230. A similar interpretation is applicable to the sedimentary basin between km 255 and 295 for profile AWI-20030500. The seismic velocities in the lower part of the basin (3–6 km depth) show the same range of values (Fig. 10) as described above. Hinz *et al.* (1987) identified two sequences of SDRs on profile 61 north of profile AWI-20030500 (Fig. 2), a landward sequence projecting onto km 245–255, and an outer sequence onto km 295–300. These locations correlate with our modelled termination of the sub-Cenozoic layer for the inner ones in and with the first clearly identified spreading anomaly C21 for the outer ones (Fig. 12) in 3–6 km depth. However, we assume that the low velocities of the deep sedimentary basin between km 255 and 295 (Figs 12 and 14) are likely to be the result of volcanic intrusions or sills that may have formed at the same time as the emplacement of the SDRs. We discuss this relationship further in the next section. We suggest that the COT terminates east of the inner SDRs at km 255 because the outer location of SDRs correlates with C21 (Fig. 12).

(2) The weakening of the short wavelength magnetic anomalies correlates with increasing depths to the high velocity gradient layers (Figs 3, 11 and 12) and the area of the COT zone is dominated

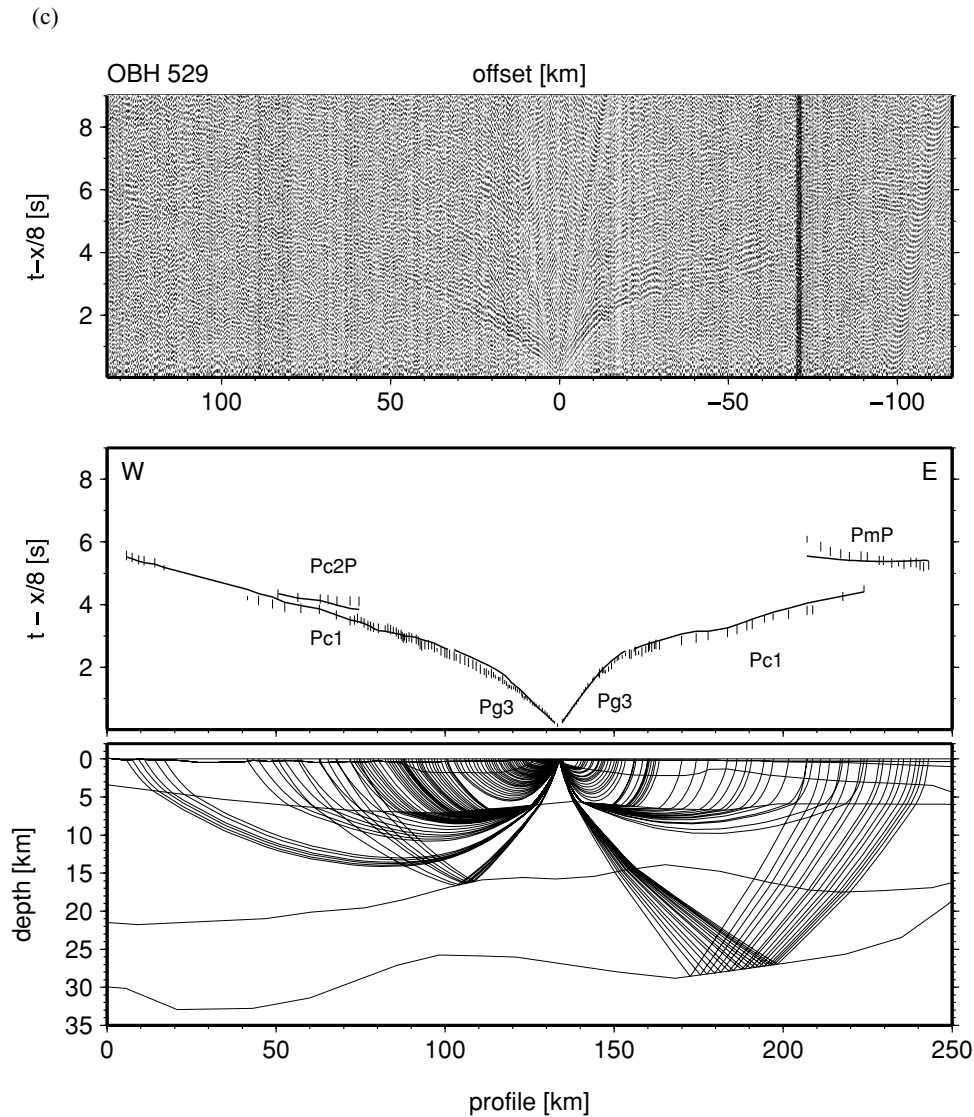


Figure 8. (Continued.)

by discontinuous magnetic anomalies with wavelengths of tens of kilometres. In our model the COT zone was formed during a long lasting rift event, which might have had a duration of several million years. During this time Late Cretaceous sediments as well as volcanic material was deposited. While the seismic velocities show an abrupt change at the boundary of this layer, we suggest that it consists mainly out of basalts. This is confirmed through the existence of a volcanic structure at km 180 of profile AWI-20030500 and the basaltic extrusive layer of profile AWI-20030400 as described above. However, the amount of syn-rift sediments compared to the basalts is unknown. The strong velocity gradient in the up to 4.5-km thick layers ($\sim 0.5 \text{ km s}^{-1} \text{ km}^{-1}$ average of both profiles) might suggest that volcanic material dominates. Thus, the long wavelength magnetic anomalies in the transitional zone might originate most likely from this basaltic layer and probably also from middle crustal intrusions. It might have formed before its subsidence together with the onshore basaltic rocks a large volcanic province.

(3) Higher crustal velocities, of 6.4 to 6.9–7.0 km s^{-1} , compared to 6.45 km s^{-1} for the global average in continental crust (Christensen & Mooney 1995) seem to support an interpretation of magmatically intruded crust in the COT. The significant increase of

the velocities in the crystalline crust correlates with the location of the short wavelengths magnetic anomalies and the pronounced negative anomaly (Figs 3, 9 and 10). Thus, we suggest to locate the landward termination of the COT at km 100 for profile AWI-20030400 and at km 130 for profile AWI-20030500. The high velocity (7.15–7.4 km s^{-1}) in the lower crustal layer has previously been interpreted as the result of Tertiary magmatic underplating (Schlindwein & Jokat 1999). A detailed discussion is provided in the next section.

(4) The pronounced Moho topography on profile AWI-20030500 and the steep increase in Moho depth along profile AWI-20030400 indicates further stretching, and crustal thinning from ~ 30 km to less than 15 km.

(5) The intermittent lower crustal reflector, already identified in the continental crustal unit of profile AWI-20030400, merges with the Moho at the seaward end of the transitional unit. Similar reflectors were identified, with gaps, along profile AWI-20030500, and by Schlindwein & Jokat (1999).

(6) The first clearly identified seafloor spreading anomalies are C22 and C21 (Figs 3, 11 and 12), marking the beginning of normal oceanic crustal accretion.

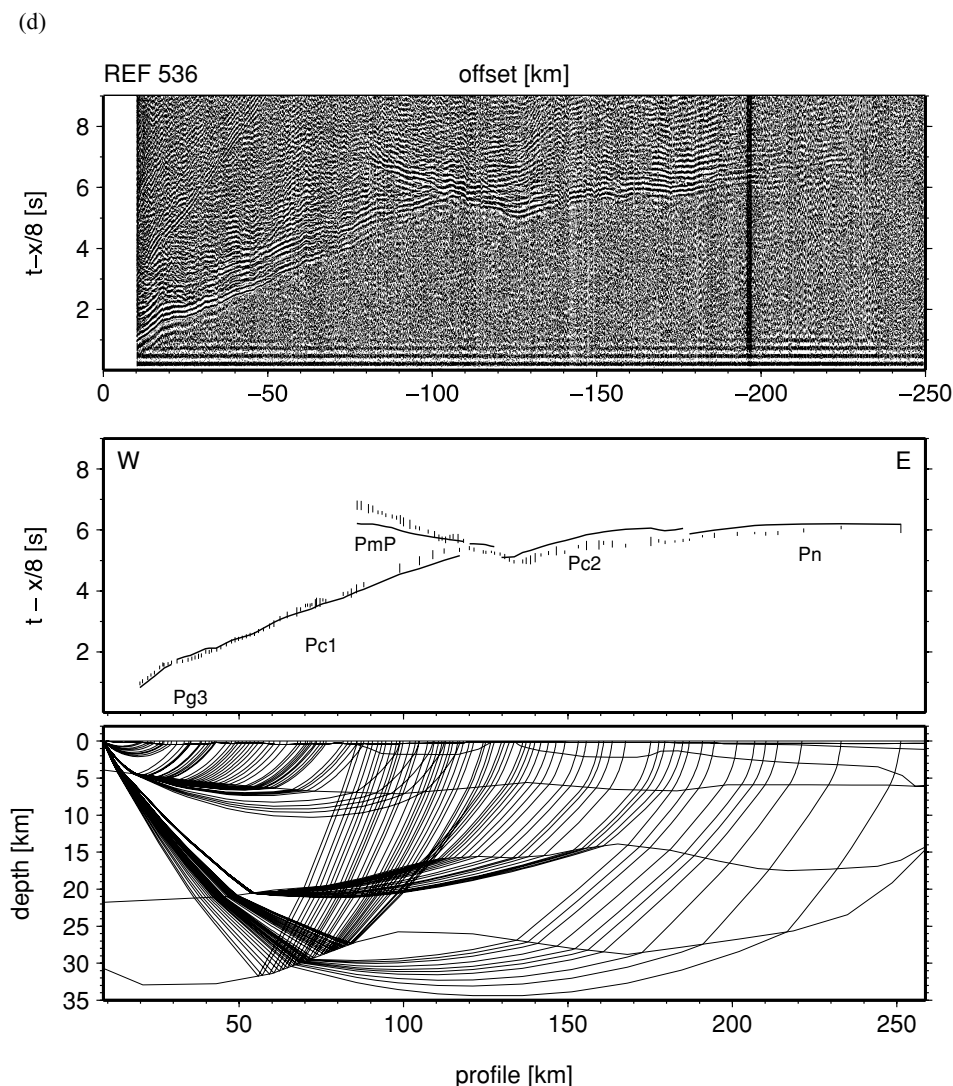


Figure 8. (Continued.)

Scott (2000) placed the COB near our landward termination of the COT (Fig. 13). His arguments were based on magnetic lineations that he interpreted as evidence for oceanic crust. Scott (2000) attributed the incoherency of the lineations to thick Cenozoic sediments overlying the area, and to be overprinted by intrusions associated with the separation of the Jan Mayen block from the East Greenland margin. Our data confirm the presence of up to 3–5 km thick Cenozoic sediments across the shelf region, and do not preclude a magmatic influence of the Jan Mayen break-up in that area. However, the seismic data reveal a concealed basaltic and syn-rift sedimentary layer extending close to the proposed location of SDRs (Hinz *et al.* 1987), which rest on highly extended continental crust.

The COB of Tsikalas *et al.* (2002), based mainly on plate reconstructions, is located 50–70 km west of C22, near OBH 417 on profile AWI-20030400 and OBH 521 on profile AWI-20030500 (Fig. 13). The profiles show no distinct structural changes in the seismic velocity models in this area and thus, do not support a COB at that location.

The above summaries of the structure of the transitional area and of the COB controversy lead us to conclude that it is only possible to define a COT at the East Greenland margin. According to

Schindwein & Jokat (1999), tectonic activity shifted from west to east in Mesozoic times and led to crustal extension. These authors proposed crustal thinning, magmatic intrusion and underplating continued into Tertiary times. The transitional zones of both profiles contain evidence for all these processes. The near surface magmatic intrusions interpreted from magnetic data, and the increase of upper crustal velocities from west to east, provide constraints on the landward limit of the COT. For the seaward termination of the COT, we applied the definition of Hinz (1981), that the eruption of SDRs occurs over highly extended continental crust during the final phases of rifting. The projection of Hinz *et al.*'s (1987) SDRs onto our profiles, and the presence of magnetic spreading anomalies C22 and C21, constrain the seaward edges of the COTs along the seismic profiles. Thus, we propose a COT width of 125 km on profile AWI-20030400 (km 100–225) and also 125 km on profile AWI-20030500 (km 130–255). The total crustal thicknesses of the COTs decrease from west to east from 29 to 13 km (AWI-20030400) and 27 to 10 km (AWI-20030500), respectively. There is no evidence on either profile for either rotated fault blocks to shift the landward boundaries of the COTs further east, or SDRs/oceanic crust to shift the seaward termination further west.

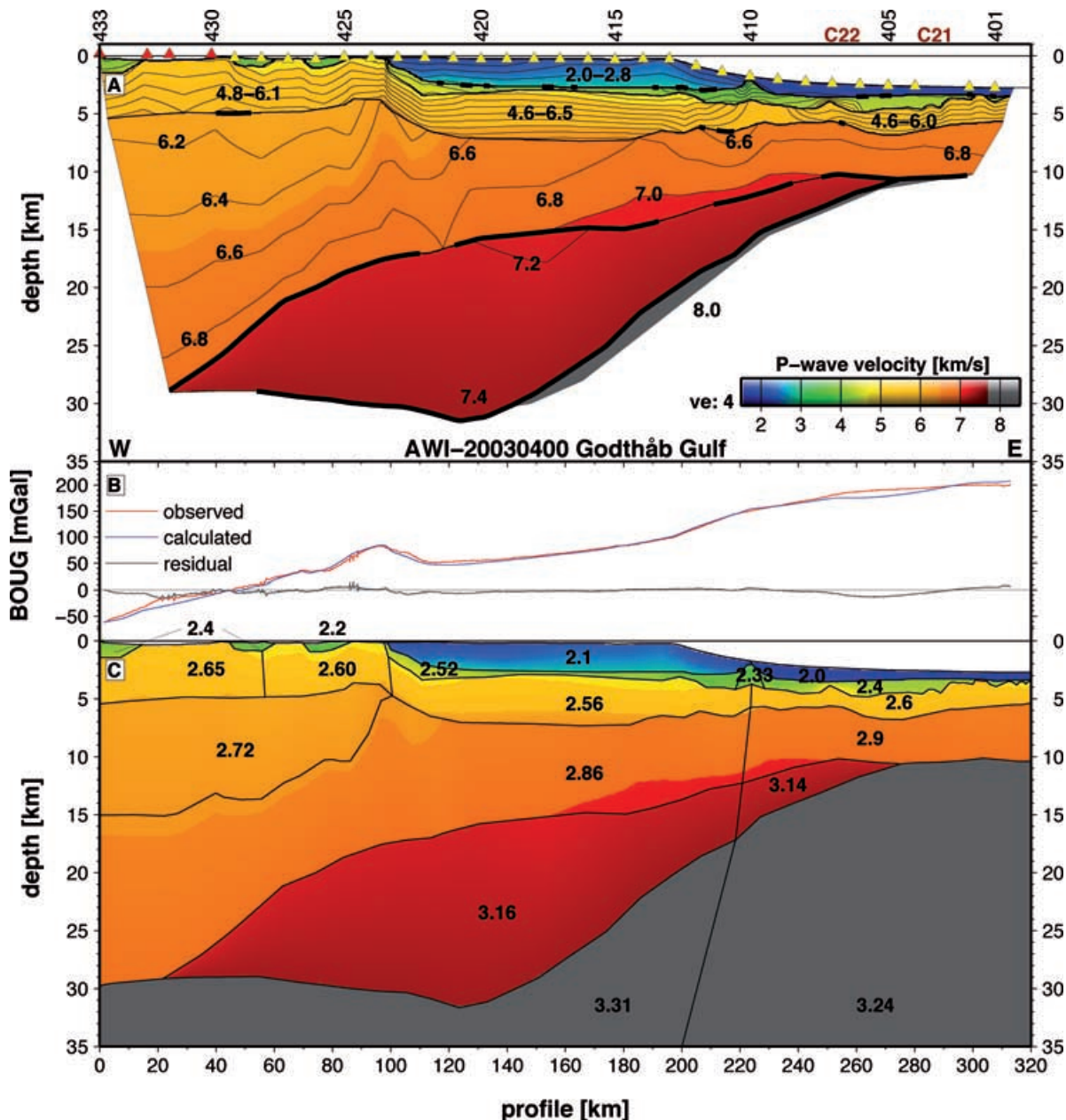


Figure 9. (A) Interpolated P -wave velocity model for profile AWI-20030400. Contour lines are from 1.6 to 7.4 km s⁻¹ every 0.2 km s⁻¹. Selected contours are individually labelled. Reflectors are marked by thick black lines. The minimum and maximum velocities are shown in the upper layers. See text for other areas with no velocities labelled. Triangles show receiver locations. C21 and C22 mark the position of magnetic ocean spreading anomalies (Fig. 3). Vertical exaggeration is 4 and comparable to Figs 10–12. The model is only shown where it is constrained by rays. (B) Observed and calculated Bouguer gravity anomalies given in mGal. Black line shows residuals. (C) 2-D gravity modelling for profile AWI-20030400. Background shows velocity grid as above. Black lines mark density polygons. Velocity layers were split into individual polygons where appropriate. P -wave velocities were converted to density using a formal approximation after Ludwig *et al.* (1970). Water was assigned with 2.67 g cm⁻³ and no terrain correction was applied within the fjord. Densities are given in g cm⁻³.

COT zones for volcanic rifted margins have a wide range in width. Seismic profiles from southeast Greenland reveal a range of 50–70 km (Holbrook *et al.* 2001) and only up to 50 km is reported from the Norwegian margins (Kodaira *et al.* 1995; Mjelde *et al.* 2001; Mjelde *et al.* 2005). Wider transition zones of 80–100 km are reported from the U.S. Atlantic margin (Holbrook *et al.* 1994a,b) and 150–200 km wide from the Namibia margin (Bauer *et al.* 2000). In contrast, the COT of the East Greenland volcanic margin is also exceptionally wide and the landward and seaward boundaries cannot

be unequivocally identified. However, the architecture of the East Greenland transition zone mirrors exceptional and long-lived rifting prior to break-up.

5.3 The oceanic crust

Clearly identifiable magnetic spreading anomalies mark the onset of oceanic crust along both profiles (Fig. 3). Paleocene–Eocene sediments (Figs 11 and 12) conceal the basement layers, which can

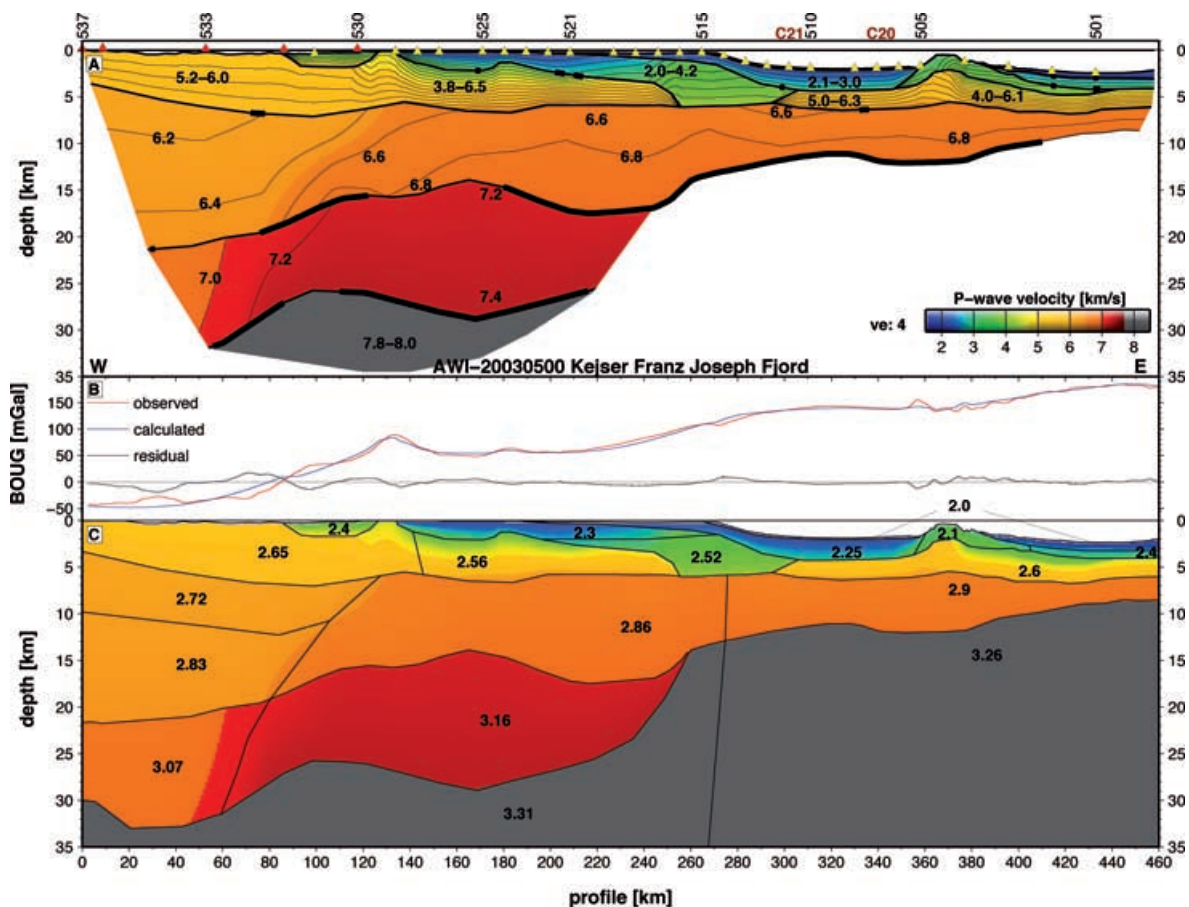


Figure 10. (A) Interpolated P -wave velocity model for profile AWI-20030500. Model descriptions are as in Fig. 9. C20 and C21 mark position of magnetic ocean spreading anomalies. (B) Observed and calculated Bouguer gravity anomalies given in mGal. Black line shows residuals. (C) 2-D gravity modelling for profile AWI-20030500. Model descriptions are as in Fig. 9C.

be related to typical oceanic layers 2 and 3 due to their seismic velocities and velocity gradients.

On profile AWI-20030400, the magmatic underplating merges into a lower oceanic layer, with velocities consistent with layer 3B (Fowler 2005), between km 230 and 270 (Fig. 11). The oceanic crust is ~ 11 km thick east of the volcanic basement high (km 230) and thins further eastward to 7 km near anomaly C21. But in this part of the layer it is impossible to establish a boundary between the magmatic underplating and oceanic layer 3B.

The oceanic crustal thickness along profile AWI-20030500 varies within the mean range of 4.8–7 km but increase to a maximum of 11.5 km beneath the ridge. The ridge is linked to the Jan Mayen Fracture Zone (Fig. 1). The velocity model is consistent with a volcanic character. A thick pile of low velocity sediments is located between the termination of the Mesozoic sediments and the onset of normal oceanic crust (km 255–295). Velocities increase slowly, to 4.2 km s^{-1} in 6 km depth, with a strong contrast to 6.6 km s^{-1} below. Similar velocities were obtained from Profile 61 (Hinz *et al.* 1987; Mutter & Zehnder 1988) in the vicinity of this region (Fig. 2) and SDRs east and west of it. Mutter & Zehnder (1988) classified also this region also as oceanic crust. A projection of spreading anomaly C22, as shown by Tsikalas *et al.* (2002), falls into the same region. The new seismic data give reasonable witness of the presence of 6–7 km thick oceanic crust based on the Moho depth in 12–14 km but an oceanic layer 2 could not be identified due to strong reverberations. We do not preclude the presence of such a layer but if it is present,

it must be very thin with a strong velocity gradient. However, a precise identification of an anomaly C22 from the magnetic data (Fig. 3) between km 255 and 295 on profile AWI-20030500 is not possible owing to the weakening signal strength of the anomaly towards southwest. We suggest a relation of the magnetic anomaly to intrusions into the sedimentary basin during the emplacement of SDRs, and that this part of the profile (km 255–295) marks the earliest stage of oceanic crustal accretion, located seawards of the proposed inner SDRs (Hinz *et al.* 1987).

5.4 The lower crustal body (LCB)

A striking result of the P -wave modelling is the thick high velocity ($7.15\text{--}7.4 \text{ km s}^{-1}$) lower crustal body (LCB), underlying continental crust and the entire COT, which terminates in thickened oceanic crust. The top of the LCB and the Moho are very well constrained by numerous traveltimes arrivals (Figs 6a and c). Along profile AWI-20030400, the LCB thins gradually towards the east and west while it seems to end abruptly for profile AWI-20030500. The maximum dimensions of the LCB are shown in Table 3. Gravity modelling supports the dimensions of the LCBs with densities of $3.14\text{--}3.16 \text{ g cm}^{-3}$, which differs significantly from normal lower crustal as well as upper mantle densities. Other high velocity layers in the lower crust were interpreted as the result of serpentinized mantle (Holbrook & Kelemen 1993; Kelemen & Holbrook 1995), oceanic layer

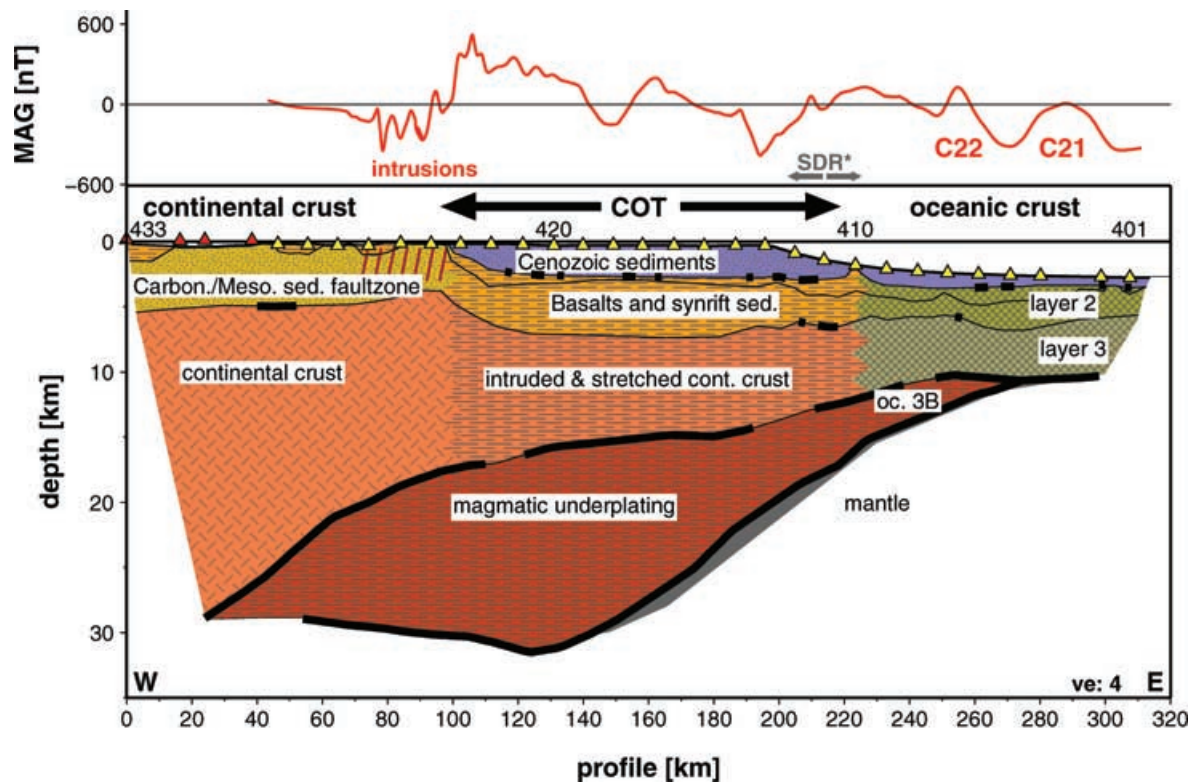


Figure 11. Bottom: Interpretation of the *P*-wave velocity model of profile AWI-20030400. Thick black lines mark wide-angle reflections. Geological units are indicated. COT: continent–ocean transition zone. oc. 3B: oceanic layer 3B. SDR*: Projection of the area of seaward dipping reflectors from profile 46 after Hinz *et al.* (1987) (see text). Parallel red lines symbolize the location of shallow intrusions as seen in the magnetic data. Different geological units are marked by different patterns. Note the wide COT and the thick magmatic underplating. Top: red curve shows projected magnetic anomalies (MAG) along the seismic line. Data derived from 5 km magnetic grid (not shown) of the newly acquired airborne data. Note the high amplitude and short wavelength variations within the area of the pronounced negative magnetic anomaly (see Fig. 2). C22 and C21 mark magnetic ocean spreading anomalies.

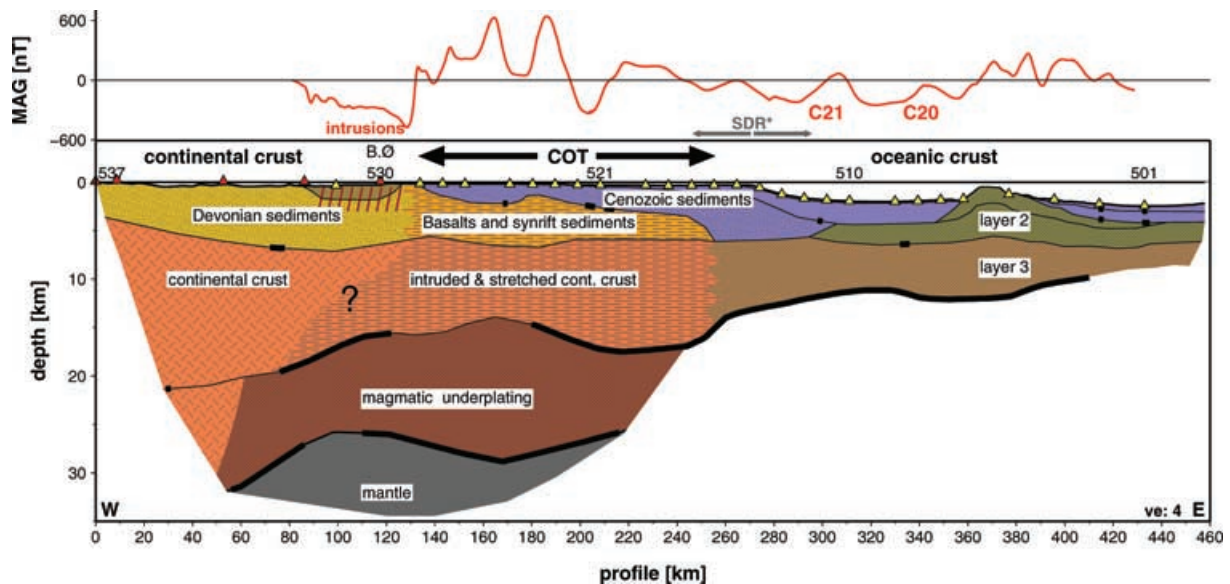


Figure 12. Interpretation of the *P*-wave velocity model of profile AWI-20030500. See Fig. 11 for descriptions. B.Ø: Bontekoe Ø. SDR*: Projection of the area of seaward dipping reflectors (see text) from profile 61 after Hinz *et al.* (1987). Large question-mark marks the questionable landward boundary of the COT within the crust due the lateral increase of seismic velocities (see Fig. 10).

3B (Mjelde *et al.* 2005) or accreted igneous material (Bauer *et al.* 2000). Schlindwein & Jokat (1999) interpreted the LCB off East Greenland as due to Tertiary magmatic underplating and suggest it coincides with a pronounced negative magnetic anomaly extending

SE–NW along the margin in the fjord region (Fig. 2). Schlindwein & Meyer (1999) show that the magnetic anomaly is most probably related to Tertiary magmatism, as the basins are intruded by Tertiary dikes and sills and partly overlain by Tertiary tholeiitic basalts

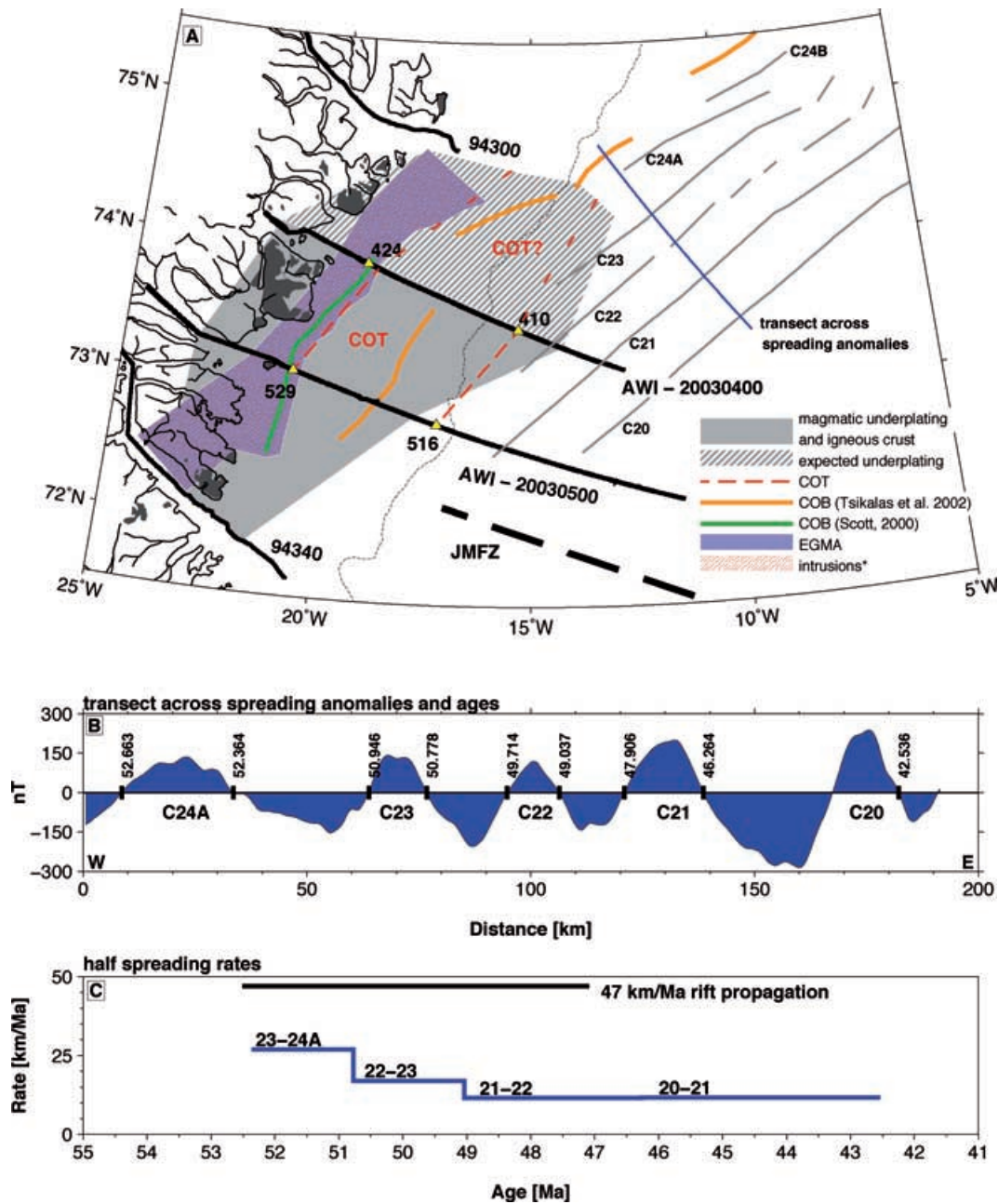


Figure 13. (A) Simplified summary of the structural results. COT: continent–ocean transition zone. COB: continent–ocean boundary. Intrusions*: Interpretation of crustal and sedimentary volcanic intrusions from short wavelength magnetic anomalies (see Fig. 3) interpolated along the negative magnetic anomaly (EGMA; East Greenland magnetic anomaly). Black lines show seismic profiles. Selected receiver locations are shown. Thin blue line shows the transect used to determine the half spreading rates (see below). Ocean spreading anomalies modified after Escher & Pulvertaft (1995) (extended to north). Black areas mark onshore basalts. (B) Magnetic wiggle along blue transect in Fig. 13A. Ages after Cande & Kent (1995). (C) Half spreading rates calculated for C24A–C21 are shown in blue. Black line shows average rift propagation velocity between C24A and C21 along their landward limits.

(Escher & Pulvertaft 1995). However, the eastward extent of the LCB remained unknown due to the lack of seismic data coverage seawards of the margin. The new data show a completely different picture of a remarkably wide and thick LCB off the East Greenland fjord region whose full extent is estimated in Fig. 13. We suggest the LCB is due to magmatic underplating that terminates eastward in a thin and immediately decreasing oceanic layer 3B. The southern termination is given by evidence for further magmatic underplating identified on profile 94340 (Schlindwein & Jokat 1999) (Fig. 2). The

negative magnetic anomaly (EGMA) terminates in a magnetic quiet zone further north, where coincidentally, no LCB was identified on seismic refraction profiles south of Shannon Island (Schlindwein 1998). The landward limits in Fig. 13 are restricted by the models after Schlindwein & Jokat (1999) and interpolated along the margin with respect to the west dipping character of the LCB on profile AWI-20030400 (Fig. 11). Thus, it is possible to interpret almost the entire shelf as being underlain by a magmatic underplate, from Kong Oscar Fjord to probably south of Shannon Island.

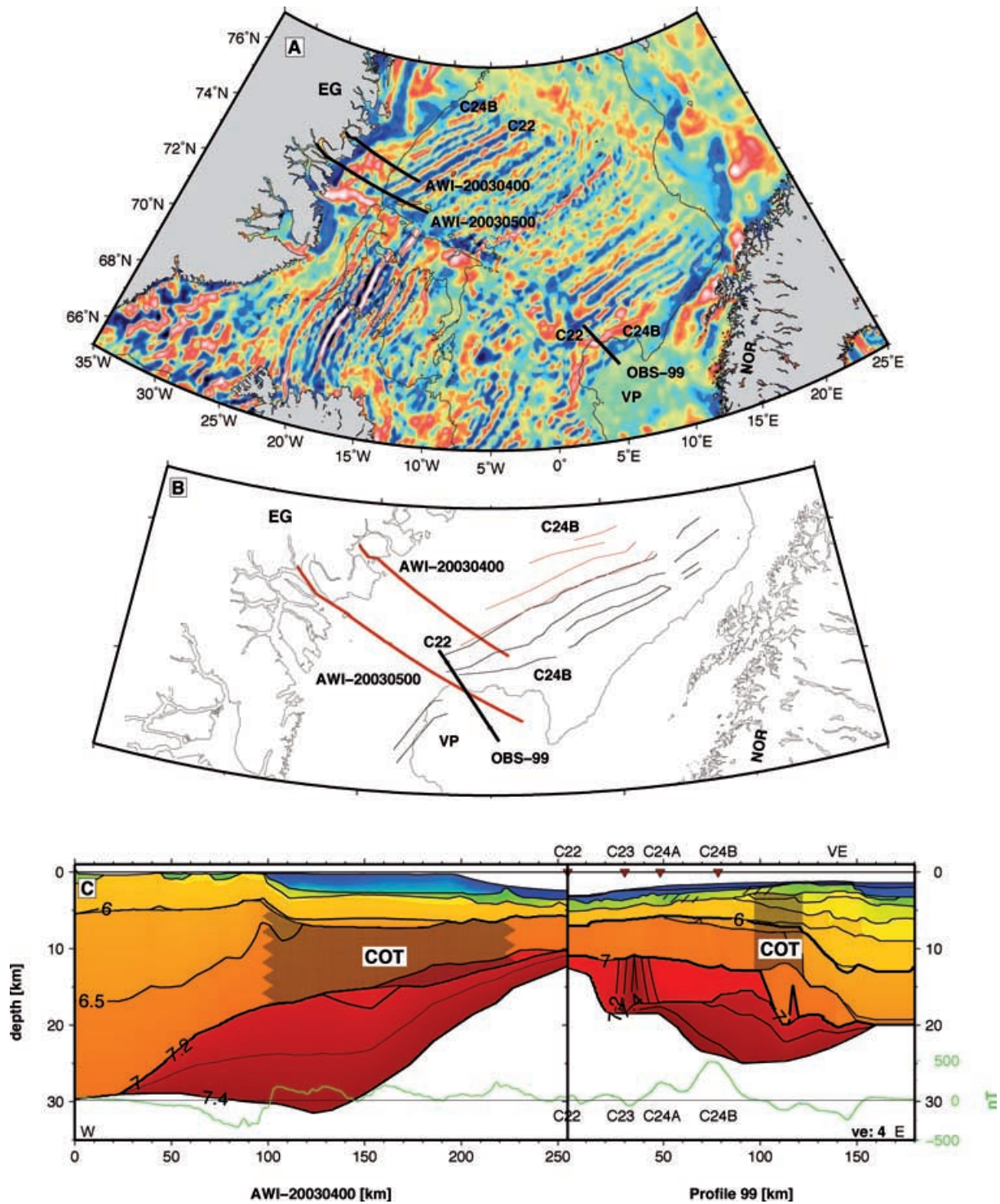


Figure 14. Comparison of the East Greenland profile AWI-20030400 and the Vøring Margin seismic profile OBS-99 after Mjelde *et al.* (2005). (A) Present-day location of seismic profiles shown as black lines. Background shows regional magnetic grid (Verhoef *et al.* 1996). White lines mark spreading anomalies. C22 and C24B are labelled. Thin black lines represent the 1500 m bathymetric contour. (B) 49.7 Ma (C22) reconstruction after Rowley & Lottes (1988). Thick lines show seismic profiles. Thin red lines mark locations of western magnetic anomalies C24B–C22. Thin black lines mark eastern spreading anomalies. The present-day 1500 m contour is shown as reference. (C) Line-up of both *P*-wave velocity models in same scale (vertical exaggeration: 4). Colours equivalent to Fig. 9. Selected contour lines are shown and labelled (6.0, 6.5, 7.0, 7.2 and 7.4 km s⁻¹). Shading marks the COTs. Green line shows regional magnetic data along the transects. Spreading anomalies are shown after Mjelde *et al.* (2005). Note the different occurrence of the anomalies on both sides. VE: Vøring Escarpment.

Table 3. Maximum widths and thicknesses of lower crustal bodies (LCB).

Profile	Width LCB	Thickness LCB	Reference
East Greenland AWI-20030400	~225 km	16 km	This paper
East Greenland AWI-20030500	~190 km	15 km	This paper
Southeast Greenland (P III)	150 km	9 km	1
Vøring Margin P99 (Fig. 12)	~150 km	12.5 km	2
US – East Coast	100–190 km	10–15 km	3, 4
Namibia	150–200 km	~18 km	5, 6
Hatton Bank	90 km	15 km	7

Notes: References for LCBs: 1 (Hopper *et al.* 2003); 2 (Mjelde *et al.* 2005); 3 (Holbrook & Kelemen 1993); 4 (Kelemen & Holbrook 1995); 5 (Gladchenko *et al.* 1998); 6 (Bauer *et al.* 2000) and 7 (Morgan *et al.* 1989).

5.5 Rift propagation

It is interesting to speculate whether underplating developed during a single event in Tertiary times, or if other pre-rift or post-break-up processes fed magma into the lower crust. On the other hand, the wide COT implicates a pinch-out of the spreading anomalies along the margin (Fig. 13) from north to south which gives rise to debate about rift propagations. Three scenarios could be possible, as follows.

Shifting of the rift-axis led to long-term rifting across the margin in the vicinity of the Kejser Franz Joseph Fjord and gave rise to the unusually wide COT in Mesozoic to Tertiary times. Direct evidence for shifts of the rift-axis can be seen in the pronounced Moho topography (Schlindwein & Jokat 1999). Several Moho slopes and plateaus exist off Kejser Franz Joseph Fjord, but the Godthåb Gulf profile shows only a steep but steady decrease of the Moho to the onset of oceanic crust. Investigations on the conjugate Lofoten and Vøring margin, off Norway, have also revealed vertical and lateral variations in crustal structure and composition resulting from a complex rifting history during the late Cretaceous and early Tertiary times (Mjelde *et al.* 1997, 1998; Raum *et al.* 2002; Mjelde *et al.* 2005; Tsikalas *et al.* 2005). The long-term rifting supported excessive upwelling of magmatic material, and intruded the stretched crust and, probably, sedimentary basins.

A second scenario involves the separation of the Jan Mayen block from East Greenland in Oligocene/Miocene times (Gudlaugsson *et al.* 1988). Scott (2000) assumed the presence of intrusions related to this event. In the first stage, Tertiary rifting was accompanied by magmatic underplating in this region (Schlindwein & Jokat 1999). Subsequently, more magmatic material was emplaced prior to the break-up of the Jan Mayen microcontinent (25 Ma). But the velocity models reveal no any evidence for two stages of emplacement, however. In such a case one might expect a reflection from inside the high velocity body, which would support this interpretation.

Another possible interpretation from the newly derived results is an episode of rift propagation from north to south, with retarded break-up and initiation of seafloor spreading in this region. The study area shows many characteristics consistent with having been part of a 'locked zone' on the spreading axis (Courtillot 1982; Vink 1982). Break-up started with chron C24B in the north and the oblique angle of the anomalies C24A, C23 and C22 along the margin between Shannon Island and the Jan Mayen Fracture Zone (Fig. 13) is consistent with a N–S rift propagation. The magnetic data provide good evidence that magnetic anomalies C24A–C21 terminate against the East Greenland COT rather than continuing beneath the shelf like in other interpretations.

Magmatic material generated during break-up remained pooled beneath the locked zone until lithospheric separation was completed in this area. Average propagation velocities of $47 \pm 5 \text{ km Ma}^{-1}$ (Fig. 13c) can be calculated from the anomaly identifications along the margin with the errors related to picking uncertainties. A preliminary calculation of the half spreading rates along a transect is shown in Figs 13a and b. The calculation relates to the zero crossings between the reversed older and normal younger anomaly. Oceanic half spreading velocities decreased from 27 to 11.7 km Ma^{-1} , which is much slower than the rift propagation. Further south of C21, younger spreading anomalies terminate towards the Mayen Fracture Zone (Fig. 2).

The existence of a wide COT and voluminous magmatic underplating is direct evidence of a long-term rifting process and rift-related magmatism. The reasons for the long-term rifting or the existence of a locked zone within a propagating rift might be related to pre-rift processes, which are not fully understood yet. Schlindwein & Jokat (1999) concluded, from the large differences of volcanic extrusion and crustal intrusions north and south of Kong Oscar Fjord, that pre-existing lithospheric structures guided the magmatic activity. However, the complexity of these tectonic and magmatic events is mirrored in the asymmetry of adjacent and conjugate margin architectures.

5.6 Competitive interpretation of the conjugate margins

A comparison of the conjugate margin structures off East Greenland and Norway provides constraints of the processes involved in the volcanic margin formation and evolution. On the conjugate margin numerous OBS profiles were acquired to investigate the crustal structure of the Vøring Plateau (Mjelde *et al.* 1997, 2001, 2005; Raum *et al.* 2002). Profile 99, across the outer Vøring Margin (Mjelde *et al.* 2005), turns out to be an adequate counterpart to profile AWI-20030400 (Fig. 14c). A reconstruction model after Rowley & Lottes (1988) with an interpolated angle of 9.68° for a C22 rotation shows a good approximation of the anomalies and a ~65 km offset of the two conjugate profiles. Thus, a comparison of the two seismic profiles of the conjugate margins should be seen as a general consideration within the limits of the reconstruction models.

Both profiles extend from continental to oceanic crust, crossing an area of complex magnetic anomalies (Figs 14a and b). Both profiles show similar crustal layering at spreading anomaly C22 (Fig. 14c), where thickened oceanic crust (~9 km) is modelled. An increase to 18.5 km towards C23 at profile 99 is in contrast to the area east of the volcanic basement high at km 225 in our model. The absence of pre-C22 magnetic anomalies in our data is a major difference between the models. On the East Greenland margin, we related the magnetic anomalies landward of C22 to strong intrusions in the stretched continental crust. If the margins were symmetrical, then profile AWI-20030400 should show anomaly C24B near km 170 (Fig. 14c). In contrast, we have presented good evidence for stretched and intruded transitional crust beneath thick Cenozoic and Mesozoic sediments at this location, rather than oceanic crust. On the other hand, the interpretation of C24B off the Vøring Margin is questionable due to the ambiguous magnetic anomaly pattern around the Vøring Plateau (Fig. 14a). The landward increase of Moho depth to ~30 km along profile AWI-20030400 is a further major difference to the Moho depth of 20 km on the conjugate margin. The eastern and western boundary structures seem similar of the COT on the conjugate profiles. The landward boundaries of the COTs are characterised by a lateral increase of seismic velocities

and thickening of the transitional crust. The seaward boundaries are located near the proposed inner SDRs. But the widths of the COTs are different. Mjelde *et al.* (2005) suggested a width of 25 km on profile 99. The East Greenland margin, however, has undergone long term stretching and, thus, the transitional zone is 125 km.

The controversy surrounding the interpretation of the magnetic anomalies significantly influences the structural models. Although local similarities in the crustal structures of the continental margin can be identified, the major and tectonically most relevant features, the COT and LCB differ greatly in their extents and thicknesses. The asymmetric crustal architecture of conjugate margins requires also a complex history of rifting and/or post-rifting events were involved but not considered so far. Further examinations of tectonic and magmatic features along the conjugate margin profiles and direct line-up comparisons could bring some more light into the processes involved in the margin formations.

6 CONCLUSION

Regional models were established along two profiles across the East Greenland continental margin between 72°N and 74.5°N. This dataset provides an insight into the lower crustal architecture in the prolongation of Godthåb Gulf and Kejser Franz Joseph Fjord. The consistency of the *P*-wave velocity models were verified by 2-D gravity modelling and were interpreted in combination with regional magnetic data and an additional improved high-resolution airborne magnetic data set. In this study, we focused on the examination of the COT and the extent of a lower crustal body associated with magmatic underplating.

One main result is the existence of a 120–130 km wide COT, that is characterized by high seismic velocities in the stretched and thinned continental crust (6.6–7.0 km s⁻¹) and by a thick high velocity lower crustal body (7.15–7.4 km s⁻¹). The maximum thicknesses of the lower crustal bodies are 15–16 km with lateral extents of 190–225 km. A well-defined intracrustal reflector is assumed to merge with the Moho in both directions. The Moho shows a distinct topography within the COT and rises from ~30 km to 11–14 km near the onset of oceanic crust. The *P*-wave velocity models reveal a concealed basaltic layer mixed with syn-rift sediments whose presence supports the interpretation of long term rifting and a highly extended transitional crust across almost the entire shelf. Given this interpretation, the presence of ocean spreading anomaly C23–C24B is unlikely between the Godthåb Gulf and Jan Mayen Fracture Zone. The magnetic anomalies are rather related to magmatic intrusions into the transitional crust and the basaltic/syn-rift sedimentary basin.

A N–S rift propagation between Shannon Island and the Jan Mayen Fracture Zone can be deduced from the SW–NE orientation of the spreading anomalies C21–C24B, and is consistent with the interpretation of tectonic and magmatic features on the seismic profiles.

Contrasting interpretations of the conjugate margin crustal structures of East Greenland and the Vøring Margin reveal significant asymmetries of the crustal architecture. The major differences are a 10 km deeper Moho in the continental unit of the East Greenland margin, a wider COT, and a larger high velocity body, interpreted as magmatic underplating rather than as oceanic layer 3B.

ACKNOWLEDGMENTS

Data acquisition along these profiles and their analyses was supported by the European Science Foundation (ESF) and the Deutsche

Forschungsgemeinschaft within the EUROMARGINS project. The manuscript improved greatly by comments from V. Schlindwein, M.C. Schmidt-Aursch, G. Eagles and also from the reviewers F. Klingelhöfer and an anonymous one. All figures were created with GMT (Wessel & Smith 1998). Magnetic data processing and 2-D gravity modelling was performed with the commercial software LCT provided by Fugro.

REFERENCES

- Bauer, K. *et al.*, 2000. Deep structure of the Namibia continental margin as derived from integrated geophysical studies, *J. Geophys. Res.*, **105**(B11), 25 829–25 853.
- Breivik, A.J., Verhoef, J. & Faleide, J.J., 1999. Effect of thermal contrast on gravity modelling at passive margins: Results from the western Barents sea, *J. Geophys. Res.*, **104**(B7), 15293–15311.
- Cande, S.C. & Kent D.V., 1995. Revised calibration of the geomagnetic polarity timescale for the Late Cretaceous and Cenozoic, *J. Geophys. Res.*, **100**(B4), 6093–6095.
- Christensen, N.I. & Mooney W.D., 1995. Seismic velocity structure and composition of the continental crust: A global view, *J. Geophys. Res.*, **100**(B7), 9761–9788.
- Courtillot, V., 1982. Propagating rifts and continental breakup, *Tectonics*, **1**(3), 239–250.
- Escher, J. & Pulvertaft, T., 1995. Geological Map of Greenland, 1:2 500 000, *Geological Survey of Greenland*.
- Fechner, N. & Jokat, W., 1996. Seismic refraction investigations on the crustal structure of the western Jameson Land basin, east Greenland, *J. Geophys. Res.*, **101**(B7), 15 867–15 881.
- Fowler, C.M.R., 2005. The solid earth: An introduction to global geophysics, 2nd ed.
- Gladchenko, T.P., Skogseid, J. & Eldholm, O., 1998. Namibia volcanic margin, *Marine Geophys. Res.*, **20**, 313–341.
- Gudlaugsson, S.T., Gunnarson, K., Sand, M. & Skogseid, J., 1988. Tectonic and volcanic events at the Jan Mayen Ridge microcontinent. *Early Tertiary Volcanism and the Opening of the NE Atlantic*. Vol. 39, pp. 85–93, eds. A.C. Morton & Parson L.M., Geological Society Special Publication.
- Henriksen, N., Higgins, A., Kalsbeek, F. & Pulvertaft, T., 2000. Greenland from Archaean to Quaternary; descriptive text to the geological map of Greenland, 1: 2 500 000, *Geol. Greenland Surv. Bull.*, **185**, 1–93.
- Hinz, K., 1981. A hypothesis on terrestrial catastrophes wedges of very thick oceanward dipping layers beneath passive continental margins; their origin and palaeoenvironmental significance, *Geologisches Jahrbuch*, **E2**, 3–28.
- Hinz, K., Mutter, J.C., Zehnder, C.M. & Group, N.S., 1987. Symmetric conjugation of continent-ocean boundary structures along the Norwegian and East Greenland margins, *Mar. Petrol. Geol.*, **3**, 166–187.
- Holbrook, W.S. & Kelemen, P.B., 1993. Large igneous province on the US Atlantic margin and implications of magmatism during continental breakup, *Lett. Nature*, **364**, 433–436.
- Holbrook, W.S. *et al.*, 2001. Mantle thermal structure and active upwelling during continental breakup in the North Atlantic, *Earth Planet. Sci. Lett.*, **190**, 251–266.
- Holbrook, W.S., Purdy, G.M., Sheridan, R.E., Glover, L. III, Talwani, M., Ewing, J. & Hutchinson, D., 1994b. Seismic structure of the U.S. Mid-Atlantic continental margin, *J. Geophys. Res.*, **99**(B9), 17 871–17 891.
- Holbrook, W.S., Reiter, E.C., Purdy, G.M., Sawyer, D., Stoffa, P.L. & Makris, J., 1994a. Deep Structure of the U.S. Atlantic continental margin, offshore South Carolina, from coincident ocean bottom and multichannel seismic data, *J. Geophys. Res.*, **99**(B5), 9155–9178.
- Hopper, J.R., Dahl-Jensen, T., Holbrook, W.S., Larsen, H.C., Lizarralde, D., Korenaga, J., Kent, G.M. & Kelemen, P.B., 2003. Structure of the SE Greenland margin from seismic reflection and refraction data: implications for nascent spreading center subsidence and asymmetric crustal accretion during North Atlantic opening, *J. Geophys. Res.*, **108**(B5), 2269.

- Jakobsson, M., Cherkis, N.Z., Woodward, J., Macnab, R. & Coakley, B., 2000. New grid of Arctic bathymetry aids scientists and mapmakers, *EOS Trans. Am. Geophys. Union*, **81**, 89, 93, 96.
- Jokat, W. *et al.*, 2004. Marine geophysics, *Reports on Polar and Marine Res.*, **475**, 11–34.
- Kelemen, P.B. & Holbrook, W.S., 1995. Origin of thick, high-velocity igneous crust along the U.S. East Coast Margin, *J. Geophys. Res.*, **100**(B7), 10077–10094.
- Kodaira, S. *et al.*, 1995. Crustal structure of the Lofoten continental margin, off N. Norway, by OBS refraction studies, *Geophys. J. Int.*, **121**, 907–924.
- Larsen, H.C. & Marcussen, C., 1992. Sill-intrusion, flood basalt emplacement and deep crustal structure of the Scoresby Sund region, east Greenland. *Magmatism and the Causes of Continental Break-up*, Vol. 68, pp. 365–386, eds Storey B.C., Alabaster T. & Pankhurst R.J., Geological Society Special Publication.
- Ludwig, W.J., Nafe, J.E. & Drake, C.L., 1970. Seismic refraction. *The Sea*. M.A.E., Vol. 4, pp. 53–84, Wiley-Interscience, John Wiley, New York, USA.
- Mandler, H. & Jokat, W., 1998. The crustal structure of central east Greenland: Results from combined land-sea seismic refraction experiments, *Geophys. J. Int.*, **135**, 63–76.
- Mjelde, R. *et al.*, 1998. Crustal structure of the northern part of the Vøring Basin, mid-Norway margin, from wide-angle seismic and gravity data, *Tectonophysics*, **293**, 175–205.
- Mjelde, R. *et al.*, 2001. Crustal structure of the outer Vøring Plateau, offshore Norway, from ocean bottom seismic and gravity data, *J. Geophys. Res.*, **106**(B4), 6769–6791.
- Mjelde, R., Kodaira, S., Shimamura, H., Kanazawa, T., Shiobara, H., Berg, E.W. & Riise, O., 1997. Crustal structure of the central part of the Vøring Basin, mid-Norway margin, from ocean bottom seismographs, *Tectonophysics*, **277**, 235–257.
- Mjelde, R., Raum, T., Myhren, B., Shimamura, H., Murai, Y., Takanami, T., Karpuz, R. & Naess, U., 2005. Continent-ocean transition on the Vøring Plateau, NE Atlantic, derived from densely spaced ocean bottom seismometer data, *J. Geophys. Res.*, **110**.
- Morgan, J.V., Barton, P.J. & White, R.S., 1989. The Hatton Bank continental margin-III. Structure from wide-angle OBS and multichannel seismic refraction profiles, *Geophys. J. Int.*, **98**, 367–384.
- Mutter, J.C. & Zehnder, C.M., 1988. Deep crustal and magmatic processes: the inception of seafloor spreading in the Norwegian-Greenland Sea, *Geol. Soc. Spec. Publ. Lond.*, **39**, 35–48.
- Nafe, J.E. & Drake, C.L., 1957. Variations with depth in shallow and deep water marine sediments of porosity, density and the velocity of compressional and shear waves, *Geophysics*, **22**, 523–552.
- Raum, T. *et al.*, 2002. Crustal structure of the southern part of the Vøring Basin, mid-Norway margin, from wide-angle seismic and gravity data, *Tectonophysics*, **355**, 99–126.
- Rowley, D.B. & Lottes, A.L., 1988. Plate-kinematic reconstructions of the North Atlantic and Arctic: late Jurassic to present, *Tectonophysics*, **155**, 73–120.
- Saunders, A.D., Fitton, J.G., Kerr, A.C., Norry, M.J. & Kent, R.W., 1997. The North Atlantic Igneous Province. *Large Igneous Provinces*, Vol. 100, pp. 45–94, eds Mahoney J.J. & Coffin M.F., American Geophysical Union Monograph.
- Schindwein, V., 1998. Architecture and evolution of the continental crust of east Greenland from integrated geophysical studies, *Reports on Polar and Marine Res.*, **270**, 1–148.
- Schindwein, V. & Jokat, W., 1999. Structure and evolution of the continental crust of northern east Greenland from integrated geophysical studies, *J. Geophys. Res.*, **104**(B7), 15 227–15 245.
- Schindwein, V. & Jokat, W., 2000. Post-collisional extension of the East Greenland Caledonides: a geophysical perspective, *Geophys. J. Int.*, **140**, 559–567.
- Schindwein, V. & Meyer, W., 1999. Aeromagnetic study of the continental crust of northeast Greenland, *J. Geophys. Res.*, **104**(B4), 7527–7537.
- Schmidt-Aursch, M. & Jokat, W., 2005. The crustal structure of central East Greenland-I: from the Caledonian orogen to the Tertiary igneous province, *Geophys. J. Int.*, **160**, 736–752.
- Scott, R.A., 2000. Mesozoic-Cenozoic evolution of east Greenland: implications of a reinterpreted continent-ocean boundary location, *Polarforschung*, **68**, 83–91.
- Tsikalas, F., Eldholm, O. & Faleide, J.I., 2002. Early Eocene sea floor spreading and continent-ocean boundary between Jan Mayen and Senja fracture zones in the Norwegian-Greenland Sea, *Marine Geophys. Res.*, **23**, 247–270.
- Tsikalas, F., Eldholm, O. & Faleide, J.I., 2005. Crustal structure of the Lofoten-Vesterålen continental margin, off Norway, *Tectonophysics*, **404**, 151–174.
- Upton, B.G.J., 1988. History of Tertiary igneous activity in the N Atlantic borderlands, *Geol. Soc. Spec. Publ. Lond.*, **39**, 429–453.
- Upton, B.G.J., Emeleus, C.H. & Hald, N., 1980. Tertiary volcanism in the northern E Greenland: Gauss Halvø and Hold with Hope, *J. geol. Soc. Lond.*, **137**, 491–508.
- Verhoef, J., Roest, W.R., Macnab, R., Arkani-Hamed, J., and Members of the 1996. Magnetic anomalies of the Arctic and North Atlantic Oceans and adjacent land areas: Open File 3125, *Geol. Surv. Canada*.
- Vink, G.E., 1982. Continental rifting and the implications for plate tectonic reconstructions, *J. Geophys. Res.*, **87**(B13), 10 677–10 688.
- Weigel, W. *et al.*, 1995. Investigations of the east Greenland continental margin between 70° and 72°N by deep seismic sounding and gravity studies, *Marine Geophys. Res.*, **17**, 167–199.
- Wessel, P. & W. Smith, H.F., 1998. New, improved version of Generic Mapping Tools released, *EOS Trans. Am. Geophys. Union*, **79**(47), pp. 579.
- White, R.S. & McKenzie, D., 1989. Magmatism at rift zones: The generation of volcanic continental margins and flood basalts, *J. Geophys. Res.*, **94**(B6), 7685–7729.
- White, R.S., McKenzie, D. & O’Nions, R.K., 1992. oceanic crustal thickness from seismic measurements and rare earth element inversions, *J. Geophys. Res.*, **97**(B13), 19683–19715.
- Whitmarsh, R.B. & Miles, P.R., 1995. Models of the development of the West Iberia rifted continental margin at 40°30’N deduced from surface and deep-tow magnetic anomalies, *J. Geophys. Res.*, **100**(B3), 3789–3806.
- Zelt, C.A. & Smith, R.B., 1992. Seismic Traveltime inversion for 2-D crustal velocity structure, *Geophys. J. Int.*, **108**, 16–34.